SEDIMENTOLOGY the journal of the International Association of Sedimentologists

Sedimentology (2022) **69**, 1179–1208 doi: 10.1111/sed.12942

Sedimentology of a hypertidal point bar (Mont-Saint-Michel Bay, north-western France) revealed by combining lidar time-series and sedimentary core data

MARTA COSMA[1,*], DIMITRI LAGUE†, ANDREA D'ALPAOS*, JEROME LEROUX†‡, BAPTISTE FELDMANN§ and MASSIMILIANO GHINASSI*

**Department of Geosciences, University of Padova, Via G. Gradenigo, 6, Padova, 35131, Italy (E-mail: marta.cosma@igg.cnr.it)*

†CNRS, Géosciences Rennes, Université de Rennes, 263 Avenue Général Leclerc, Rennes, 35042, France

‡Geofit Expert, 1 Route de Gachet, Nantes, 44 307, France

§CNRS, Observatoire des Sciences de l'Univers, Université de Rennes, 263 Avenue Général Leclerc, Rennes, 35042, France

Associate Editor – Piret Plink-Björklund

ABSTRACT

Intertidal meanders developed on salt marshes are known to expand and produce inclined heterolithic stratification rich in fine-grained sediments and to bear evidence for rhythmic deposition in the upper part of the inner meander bend (i.e. the upper part of the point bar). This occurs because the lower point-bar deposits are washed by strong currents, which remove mud drapes and develop discontinuous record of tidal cycles. Although these criteria are widely accepted, facies models for tidal point bars still lack a three-dimensional perspective and overlook the along-bend variability of sediment distribution. The present study focuses on a hypertidal point bar belonging to the upper-intertidal domain of the Mont-Saint-Michel Bay (France), and it analyses the sedimentology of a 3D time-framed accretionary package formed between 28 March 2012 and 29 November 2012 by means of lidar topographic data, geomorphological field surveys and sedimentological core data. To define the 3D time-framed accretionary package, data from thirteen lidar (light detection and ranging) topographic surveys were used to create the point-bar synthetic stratigraphy. Data show that over the study period the point bar expanded alternating deposition along its seaward and landward sides, pointing out the occurrence of depositional patterns more complex than a simple progressive expansion of the bend. The thickest deposits were accumulated in the point-bar-apex zone, where the largest amount of mud was also stored. High sediment accretion in the bend-apex zone is ascribed to the development of low-energy conditions due to flow and bed configuration. High accretion rate of the point-bar-apex zone promoted also a better preservation of rhythmites, which are almost missing from deposits accumulated along the point-bar sides. This study remarks that preservation of mud and tidal rhythmites within intertidal-point-bar deposits is controlled, not only by their elevation with respect to the tidal range, but also by their location along the point bar.

Keywords Bidirectional flow, mutually evasive currents, rhythmites, synthetic stratigraphy, tidal meander, upper-intertidal zone.

[1]Present address: Institute of Geosciences and Earth Resources, National Research Council, Via Gradenigo, 6, 35131, Padova, Italy.

INTRODUCTION

Tidal meandering channels and related point-bar deposits have mainly been studied in modern coastal areas spanning different tidal ranges. They have been studied in the following tidal regimes (as defined by Archer, 2013): (i) microtidal (Smith, 1987; Fruergaard *et al.*, 2011; Brivio *et al.*, 2016; Ghinassi *et al.*, 2018a; Cosma *et al.*, 2019, 2021); (ii) mesotidal (Barwis, 1978; Smith, 1987; Fenies & Faugères, 1998; Sisulak & Dashtgard, 2012; Johnson & Dashtgard, 2014); (iii) macrotidal (Woodroffe *et al.*, 1986; Knighton *et al.*, 1991; Van den Berg *et al.*, 1996); and (iv) hypertidal (Bridges & Leeder, 1976; De Mowbray, 1983; Lanier & Tessier, 1998; Pearson & Gingras, 2006; Choi, 2010, 2011; Choi & Jo, 2015).

The main differentiation between tidal meandering channels is given by their location in the intertidal or subtidal zone, which cause them to be either periodically or permanently submerged, respectively [see Martinius & Van den Berg (2011) for a review]. This work focuses on the intertidal setting, particularly in the upper intertidal zone. Migration and planform evolution of tidal bends are governed by a complex interaction between hydrodynamics (i.e. changes in tidal prism, tidal asymmetry, bidirectional behaviour of tidal currents, mutually evasive ebb and flood flow pathways), substrate composition and morphology, sediment grain size, and vegetation cover (Van Veen, 1950; Ahnert, 1960; Robinson, 1960; Van Straaten, 1964; Garofalo, 1980; Leopold *et al.*, 1993; Van den Berg *et al.*, 1996; Gabet, 1998; Cleveringa & Oost, 1999; Zeff, 1999; Marani *et al.*, 2002; Solari *et al.*, 2002; Fagherazzi *et al.*, 2004; Garotta *et al.*, 2007; Li *et al.*, 2008; Carling *et al.*, 2015; D'Alpaos *et al.*, 2017; Finotello *et al.*, 2018). These processes interact at different spatial and temporal scales to shape the distribution of sedimentary facies and the stratigraphic architecture of tidal-point-bar deposits. Nevertheless, with some exceptions (Choi *et al.*, 2004, 2013; Choi & Jo, 2015), most facies models do not acknowledge such a variability, and ascribe the accretion of intertidal point bars to a progressive increase of meander-bend sinuosity (Bridges & Leeder, 1976; De Mowbray, 1983). This incompleteness of facies models is reflected in the scarce documentation of tidal point bars in the stratigraphic record (Nio & Yang, 1991; Santos & Rossetti, 2006; Musial *et al.*, 2012; Legler *et al.*, 2013; Díez-Canseco *et al.*, 2014; Olariu *et al.*, 2015; Pelletier *et al.*, 2016; Cosma *et al.*, 2020), where these deposits are essentially detected on the basis of a number of criteria, including: abundance of mud, high degree of bioturbation (brackish to marine trace fossil), rhythmic deposition, reactivation surfaces and bidirectional flows (Allen, 1982; Smith, 1987; Cuevas Gonzalo *et al.*, 1991; Gingras *et al.*, 2016).

Although rivers with high suspended load and seasonal discharge can produce mud-rich and cyclically-organized deposits (Jablonski & Dalrymple, 2016; Johnston & Holbrook, 2019; Simon *et al.*, 2019), the abundance of mud and the rhythmic deposition are commonly considered as a signature of tidal processes (Bridges & Leeder, 1976; Barwis, 1978; Boersma & Terwindt, 1981; De Mowbray, 1983; Terwindt, 1988; Kvale *et al.*, 1989; Tessier & Gigot, 1989; Choi *et al.*, 2004; Pearson & Gingras, 2006; Santos & Rossetti, 2006; Dalrymple & Choi, 2007; Hubbard *et al.*, 2011; Fustic *et al.*, 2012; Kvale, 2012; Croix & Dashtgard, 2014, 2015; Rossi *et al.*, 2017). In tidal environments, mud can occur: (i) as laminae which define sedimentary structures (Van Straaten, 1954; Reineck, 1970; Dalrymple *et al.*, 1991; Tessier, 1993; Choi, 2010, 2011; Martinius & Van den Berg, 2011); (ii) as layers (for example, fluid mud Harris *et al.*, 2004; Ichaso & Dalrymple, 2009; Longhitano *et al.*, 2012; Chen *et al.*, 2015); and (iii) as intervals within the inclined heterolithic stratification (Bridges & Leeder, 1976; Barwis, 1978; De Mowbray, 1983; Thomas *et al.*, 1987; Choi *et al.*, 2004, 2013; Fagherazzi *et al.*, 2004; Rebata-H. *et al.*, 2006; Hovikoski *et al.*, 2008; Kleinhans *et al.*, 2009; Sisulak & Dashtgard, 2012; Johnson & Dashtgard, 2014; La Croix & Dashtgard, 2014). In tidal point bars, mud is considered to be dominant in the upper-point-bar zone, and as mud-clast breccias mainly developed by failures of outer bank deposits (Reineck, 1970; Van den Berg, 1981; Musial *et al.*, 2012; Sisulak & Dashtgard, 2012; Broughton, 2018; Gugliotta *et al.*, 2018). Rhythmites showing neap–spring cycles are the most reliable evidence for tidal processes (Tessier, 1993, 1998; Lanier & Tessier, 1998; Choi & Park, 2000; Choi & Dalrymple, 2004). However, with the exception of some uniquely preserved examples (Pelletier *et al.*, 2016), distribution and preservation of these structures within tidal point bars are not ubiquitous (Choi, 2010, 2011; Choi *et al.*, 2013). Their occurrence has been investigated mainly in terms of the elevation of the point bar with respect to Mean Sea Level (MSL). In intertidal point bars (e.g. Choi, 2011), rhythmites

are preferentially formed above MSL and below Mean High Water Level (MHWL), and commonly recorded in the upper part of point-bar deposits (Tessier, 1993; Archer, 1998, 2013; Choi, 2010, 2011; Choi *et al.*, 2013; Pelletier *et al.*, 2016). Nevertheless, if the upper part of the point bar is situated in the uppermost intertidal zone, the limited number of flooding events (i.e. higher flood spring tides) prevents the development of a clear rhythmic signal (Tessier, 1993, 1998; Choi, 2011; Martinius & Van den Berg, 2011; Pelletier *et al.*, 2016). Whereas high energy conditions occurring in the lower part of the point bar prevent preservation of a rhythmic deposition there (Tessier, 1998; Choi *et al.*, 2004). Pervasive bioturbation, both by rootlets and organisms, can further decrease conservation of tidal rhythmites (Allen, 1982; Choi, 2011). In summary, distribution of mud deposits and rhythmites within tidal-point-bar deposits has been commonly discussed in terms of their elevation within the point-bar body, disregarding both the effects of tidal currents in the planform evolution of meander bends, and the along-bend variability of sedimentary processes. Furthermore, mechanisms of tidal-point-bar growth are still simplistically linked with a progressive increase of bend sinuosity, lacking a more comprehensive 3D perspective and complexity.

The present study focuses on a hypertidal point bar formed by a tidal bend situated in the upper-intertidal domain of the Mont-Saint-Michel Bay (France), and aims at better understanding the mechanisms of tide-dominated point-bar sedimentation over a timescale of several months. Sedimentary features and depositional dynamics of a time-framed accretionary package are analysed in a 3D perspective, by means of: (i) repeated lidar topographic data; (ii) geomorphological field surveys; and (iii) core data. This short timescale analysis is framed within the evolution of the meander at the decennial timescale, highlighting its role in distributing sediments and preserving tidal signature along the point bar. The along-bend distribution of sedimentary features, including grain size, thickness and preservation of tidal signature are illustrated and discussed.

STUDY AREA AND GEOLOGICAL SETTING

The Bay of Mont-Saint-Michel

The Mont-Saint-Michel Bay is located in the north-western coast of France along the English Channel (Fig. 1A). It is a hypertidal environment, with a tidal range reaching up to 15.3 m during the highest spring tides (Larsonneur, 1989; Tessier, 1993; Larsonneur *et al.*, 1994; Levoy *et al.*, 2000) and 8.5 m for mean tides (Levoy *et al.*, 2019). The tidal regime is semi-diurnal with slight periodical diurnal inequality. The bay is a wide (500 km^2) and shallow (<20 m) embayment gently dipping towards the north-west, and incised into a Precambrian substrate, belonging to the Armorican Massif. The basement rocks include variably metamorphosed folded schist intruded by granitic rocks (L'Homer *et al.*, 1999), of which the 92 m high circular outcrop of Mont-Saint-Michel is the most famous thanks to the overlying Middle Age monastery. The present-day configuration of the Mont-Saint-Michel Bay is the result of the combined action of Plio-Pleistocene glacio-eustatic fluctuations and negligible regional subsidence: the morphology of the substrate was modelled by river incision, particularly during lowstand phases; whereas the sedimentary infill of the bay was highly reworked and, nowadays, it records only the last post-glacial transgression, with only few remnants of Pleistocene fluvial terraces (Larsonneur *et al.*, 1994; L'Homer *et al.*, 1999; Billeaud *et al.*, 2007, 2009; Tessier *et al.*, 2010). Three main morpho-sedimentary domains are identified in the present-day bay (Caline *et al.*, 1982): (i) a wide sheltered embayment characterized by tidal flats towards the west; (ii) a narrow wave-dominated barrier system towards the north-east; and (iii) a huge tide-dominated estuarine system towards the south-east, where the study site is located. The Bay of Mont-Saint-Michel is dominated by tidal dynamics. Tidal-current speeds show high spatio-temporal variations, with maximum flood currents at the entrance of the bay of about 1 m s^{-1} (for mean high spring tides), which decrease towards the inner part of the bay to 0.3 to 0.7 m s^{-1} on the tidal flats. The highest speeds are recorded within intertidal channels, where currents can reach up to 2.5 m s^{-1} (Larsonneur, 1989; Leroux, 2013). The wave energy is relatively low because wave propagation is hindered by shoreface bathymetry and by the presence of the Saint Malo peninsula and the Chausey Archipelago (Fig. 1A), which protect the bay from the prevailing western and northern storms. However, severe storm waves can sometimes affect the whole bay (Larsonneur *et al.*, 1994), enhancing suspension and thus active sediment transport (Desguée *et al.*, 2011).

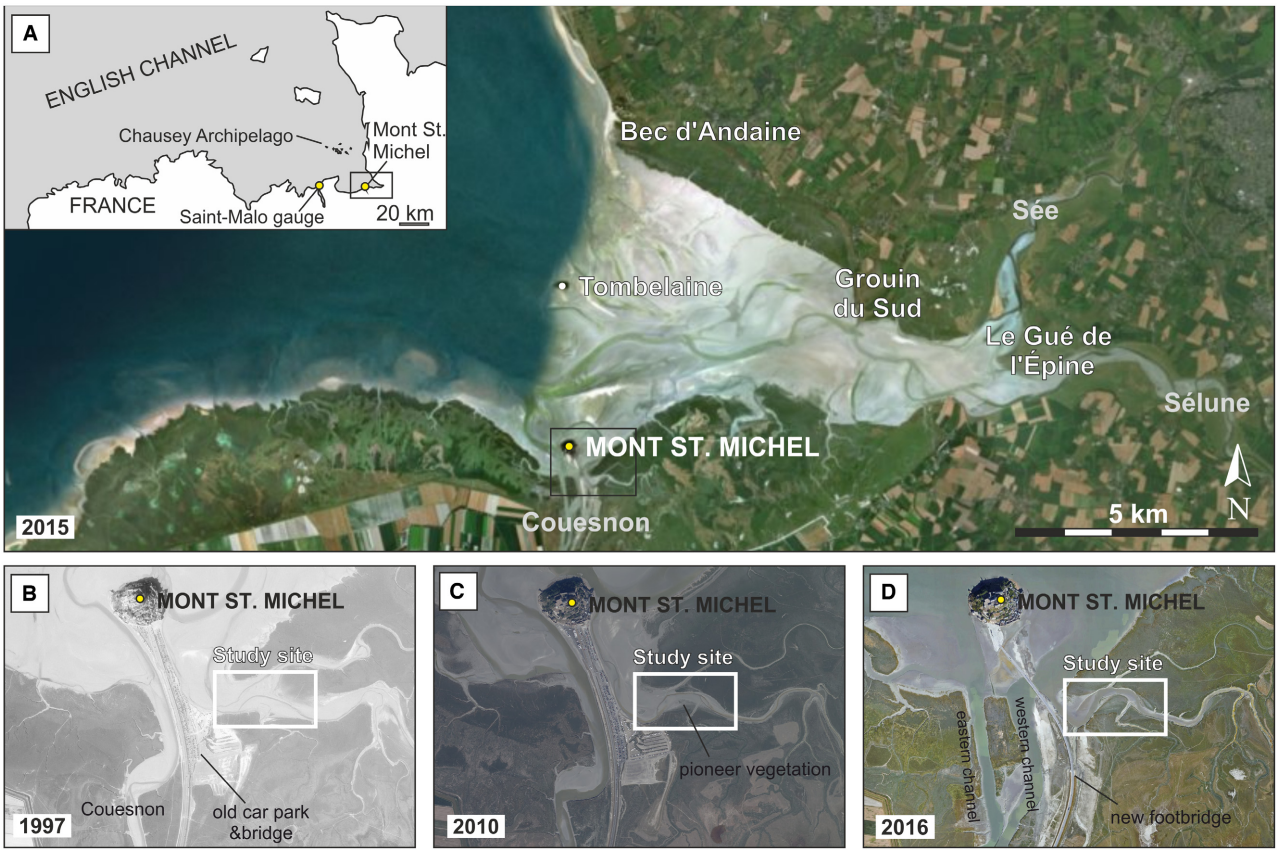

Fig. 1. The study site. (A) Geographic location of the studied meander bend within the estuarine domain of the Mont-Saint-Michel Bay. (B) to (D) Aerial photographs and satellite images of the studied meander between 1997 and 2016 showing the planform evolution of the meander and the progressive colonization of the point bar top by pioneer vegetation. Source of the satellite image: Google™ Earth (2015 and 2016); source of the aerial photograph: https://remonterletemps.ign.fr/ (1997 and 2010).

Furthermore, tidal bores are observed during spring tides in the estuarine domain, contributing to sediment resuspension and transport (Furgerot *et al.*, 2013; Tessier *et al.*, 2017). Three rivers (Sée, Sélune and Couesnon) flow into the eastern bay (Fig. 1A) and are characterized by low mean annual discharge (Larsonneur, 1989), which ranges between *ca* 10 m^3/s (Sélune and Couesnon) and 8 $m^3\ s^{-1}$ (Sée), representing 1.5% of the oscillating volume of water in the bay on an annual basis (Migniot, 1997). The annual sediment supply of these rivers is considered as negligible (Larsonneur *et al.*, 1994; Bonnot-Courtois *et al.*, 2002). Vice versa, there is a positive sediment supply from marine sources, causing a net sediment transport towards the inner part of the bay (Desguée *et al.*, 2011). Sediment grain size progressively decreases from the outer to the inner part of the estuarine domain. In the upper-intertidal zone of the estuarine domain, mean grain size ranges from very-fine sand (0.09 mm) to silt (0.03 mm – Bourcart & Charlier, 1959; Larsonneur, 1975, 1989) and consists of both a bioclastic (up to 50%) and a mineral fraction (Larsonneur, 1989; Tessier, 1993; Billeaud *et al.*, 2007).

The study site

The study site is located at the fringe of the salt marshes in the surroundings of Mont-Saint-Michel and about 500 m east of the Couesnon mouth (Fig 1). The salt marshes of this area developed in the last five decades and progressively colonized the surrounding tidal flats (Larsonneur, 1989; Bonnot-Courtois *et al.*, 2002; Desguée, 2008; Bonnot-courtois & Levasseur, 2012; Bonnot-Courtois, 2012, 2020). Salt marsh progradation, caused by the natural infilling of the bay and enhanced by anthropic intervention [see Bonnot-Courtois, (2020) for a detailed summary], was rapid and it threatened the maritime character of

Mont-Saint-Michel. Therefore, between 2006 and 2017, a series of engineering works took place, including: the substitution of the older dam, the separation of the Couesnon into two main channels downstream of the dam, the relocation of the car park on the mainland, and the installation of a footbridge allowing access to Mont-Saint-Michel without blocking the tidal flow and the Couesnon divagation (http://www.projetmontsaintmichel.com/pourquoi_agir/objectifs.html). The study site was not directly affected by these major engineering works (Leroux, 2013). Up until 2015, the dam, which stores water at high tide and releases it at low tide, was mostly affecting the area located on the west side of Mont-Saint-Michel. Only after 2015, with the opening of the second channel on the east side of Mont-Saint-Michel (Fig. 1), the dam could have started to influence flow patterns and tidal channel migration further seaward than the study site. Furthermore, the dam releases water six hours after high tide, at a time when our study channel is already completely emptied and therefore not affected by the dam operation.

The study channel during the last two decades progressively increased its sinuosity and mainly migrated seaward, as is evident from the analysis of the channel thalweg movements (Fig. 2A) based on aerial photographs (https://remonterletemps.ign.fr) and satellite images (https://earth.google.com). In particular, the planform transformation of the study meander between 1997 and 2010 consists of a series of landward (for example, between September 1997 and September 2000) and seaward (for example, between September 2002 and June 2006) shifts with an overall dominant seaward component, followed by an expansion towards the north between 2010 and 2016 (Figs 1B, 1C, 1D and 2A). Nowadays, the study meander, draining 2.2 km^2 of salt marshes, shows a radius of curvature of about 125 m, a sinuosity of *ca* 1.26 and is almost 3 m deep at bankfull stage (i.e. the water level at which any further rise would result in overflow on the marsh platform – measured as the difference between high marsh and channel thalweg elevation). Two tributary channels flow into the study bend: one on the left bank flowing towards the north-west, and the other on the right bank (i.e. outer bank) flowing towards the south-west (Fig. 1). Data derived from lidar surveys acquired between 2011 and 2017 (Leroux, 2013; Fig. 2B, C and D – see relative high tide elevation in Fig. 3A) show that elevation in the study area ranges between 4.0 (in the channel thalweg) to 7.0 (in the high marsh zone) Metres Above Mean Sea Level (MAMSL), which approximates French ordinance datum (IGN69; vertical reference is implied henceforth). The study bend is located in the upper-intertidal domain, implying that during spring tides, the channel empties out twice per day, while around neap tides, the whole channel is dry for about one week. The point-bar-top zone exhibits a clear vegetation zonation typical of the Mont-Saint-Michel Bay (Tessier *et al.*, 2000; Bonnot-Courtois *et al.*, 2002; Langlois *et al.*, 2003; Détriché *et al.*, 2011), with a permanent vegetation cover of *Halimione portulacoides* and *Festuca rubra* in the middle (*ca* 6.2–7.0 MAMSL, in the study site) and high (>7.0 MAMSL *ca*, in the study site) marsh (Fig. 2B), and a progressively less dense cover in the low marsh going from *ca* 6.2 to 4.5 MAMSL *ca*, with the presence of *Suaeda maritima, Salicornia fragilis, Pulcinella maritima* and *Spartina anglica*. Pioneer vegetation started to develop on the study meander in 2009 (Leroux, 2013), and progressively colonized the point-bar top (Fig. 1B, C and D). Specifically, between 2011 to 2013 vegetation cover mainly expanded towards the north-east, whereas between 2013 and 2017 it grew mainly towards the west (dashed lines in Fig. 2B and C). Growth pattern of vegetation also reflects the overall expansion of the point bar (Fig. 2B, C and D). The overall retreat of the outer bank (mainly towards the north-east) in this period ranges between 7 m and 15 m *ca* (solid lines in Fig. 2B and C).

Velocities of tidal currents in the study meander have been analysed by Leroux (2013) with data acquisition performed between 2010 and 2013. A large spatio-temporal variability was registered (Fig. 2E and F). During undermarsh tides (high tide elevation <7 MAMSL), the channel is neither flood-dominated nor ebb-dominated (Fig. 2E) at any tide elevation, while it tends to be ebb-dominated for overmarsh tides (high tide elevation >7 MAMSL). A tidal bore develops for overmarsh tides, but it is hardly documented by the velocity data in the channel because it occurs for tide elevations below 5 m on the site. During overmarsh tides, the seaward side of the point bar (Fig. 2F) is dominated by flood flows (directed towards ENE across the point bar), with almost null velocity recorded during ebb phase. Vice versa, at the landward side (Fig. 2F), ebb flow (*ca* 1.00 m s^{-1}) is two times larger than flood flow and is directed towards the north-west (parallel to the

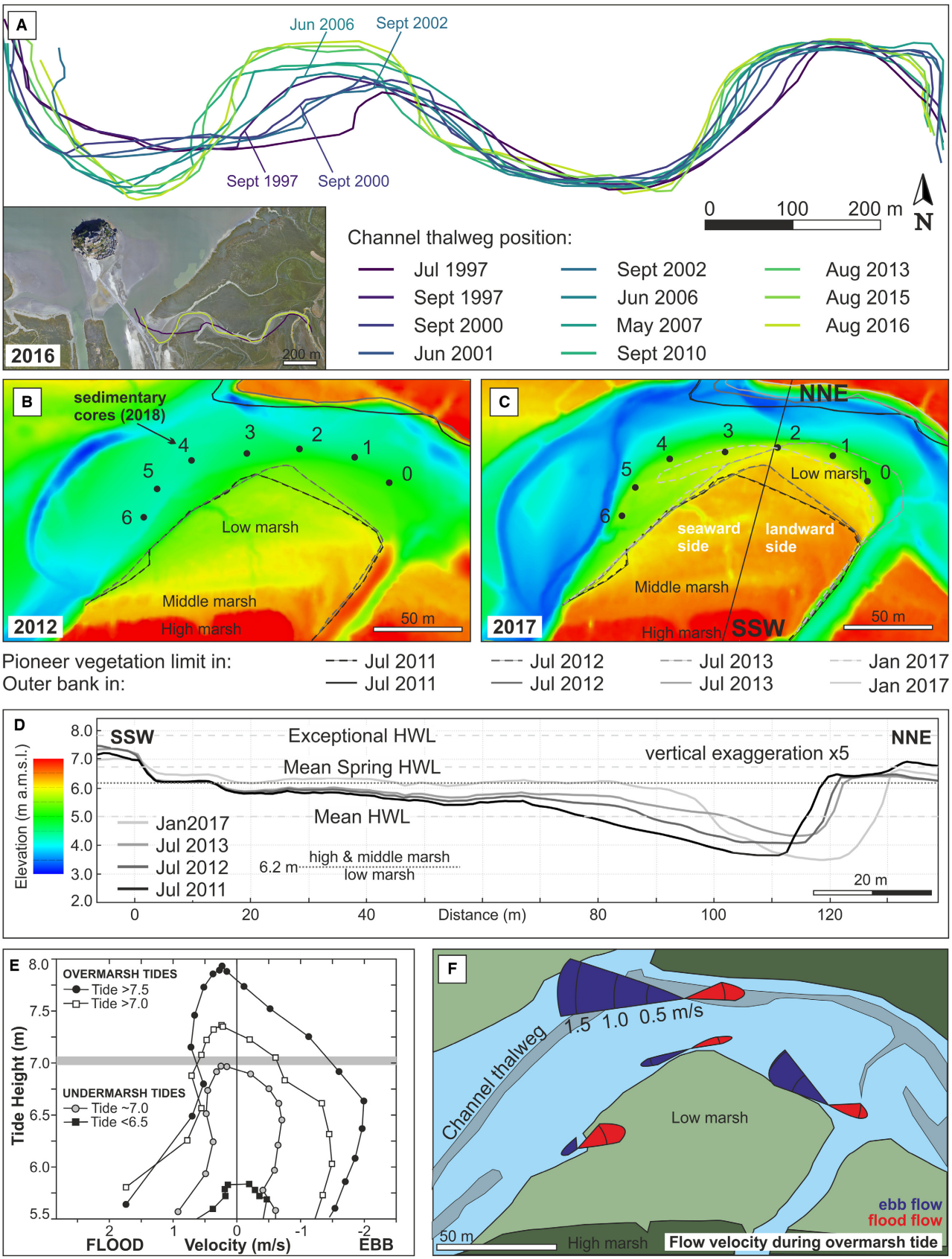

Fig. 2. (A) Long-term evolution of the study channel based on the position of the channel thalweg between 1997 and 2016. Aerial photographs and satellite images used are available at https://remonterletemps.ign.fr/ and in Google™ Earth, respectively. (B) and (C) Lidar images showing point-bar topography in 2012 (B) and 2017 (C), with the location of the vegetation limit (dashed lines) and the outer bank (solid lines) between 2011 and 2017. (D) Changes in point-bar elevation along the bend axis between 2011 and 2017. (E) Flood and ebb peak velocities at different tide stages for different overmarsh and undermarsh tides measured with an Acoustic Doppler Current Profiler (ADCP) located in the channel. The grey line at *ca* 7 Metres Above Mean Sea Level (MAMSL) indicates the elevation of high marshes and separates overmarsh (high tide elevation >7 MAMSL) and undermarsh (high tide elevation <7 MAMSL) tides. The time step between consecutive points is 10 min. Note the longer duration of the ebb phase in comparison to the flood phase, and the dominance of the ebb flow for overmarsh tides (from Leroux, 2013). (F) Flow direction and magnitude at different location in the study meander for overmarsh tide. Velocity data in the channel and in the landward and seaward sites were measured with an ADCP (showing the peak water column velocities) and two ADV (showing the near bed velocities), respectively, on 08 April 2012 (High Water Level = 7.35 MAMSL); whereas velocity data in the apex were measured with an ADV (showing the near bed velocities) on 29 March 2013 (High Water Level = 7.05 MAMSL). Data are reported from Leroux (2013).

vegetation limit). In the apex zone (Fig. 2F), flood and ebb flows are weaker (*ca* 0.75 m s^{-1}). In the channel thalweg (Fig. 2F), the highest velocities are registered for the ebb flow, exceeding 1.50 m s^{-1} (towards the west); while flood current exceeds 0.50 m s^{-1}.

METHODS

Morphodynamic evolution and sedimentology of the point bar have been characterized by means of integration between lidar surveys, ground-checking and recovery of cores. Specifically, a point-bar accretionary package accumulated between 28 March 2012 and 29 November 2012 (hereinafter termed '2012 accretionary package') has been spatially defined and cored in order to compare sedimentary products with corresponding styles of point-bar accretion and recorded variations of tidal excursion. This time interval has been selected because of the availability of nearly regularly-distributed Terrestrial Laser Scanner (TLS) surveys (acquired by Université de Rennes – Leroux, 2013), which capture changes in point-bar morphology during both neap and spring tides (Fig. 3A). This integrated approach aims at characterizing morphodynamic and sedimentological processes occurring along the seaward and landward sides (Fig. 2C) of the point bar. Methodologies used in this work are concisely described in the next paragraphs.

Topographic data sources and point-cloud processing

The topographic data consist of thirteen short-range TLS surveys and one long-range airborne lidar survey (Fig 3A). This last survey was acquired in January 2017 using a Teledyne Optech Titan lidar (Teledyne Optech, Toronto, ON, Canada) resulting in a point cloud density of 10 pts m^{-2}, with a vertical uncertainty of ±10 cm. The TLS surveys were conducted at low tide using a Leica® Scanstation 2 (Leica, Wetzlar, Germany) mounted on a survey tripod. Detailed characteristics of this scanner can be found in Lague *et al.* (2013) and Leroux (2013). For each survey, three to eight different scanning stations were used, depending on the time available between tides, and were co-registered both for intra-survey registration and for local geo-referencing using both fixed and mobile targets. Registration errors vary between 1.5 mm and 3.4 mm. As is typical of TLS data, large variations in point density occurred, ranging between 1 to 10 pts cm^{-2} in the pioneer vegetation area, and around 1 pt cm^{-2} in the outer bank. The targets were also surveyed with differential GPS at ±2 cm vertical precision to link the TLS surveys to the IGN69 reference elevation.

All the processing of lidar data, described hereinafter, was performed using CloudCompare, a 3D point cloud editing and processing software (EDF R&D, 2011). An initial treatment of the raw point clouds has been necessary to create the synthetic stratigraphy (see *Identification of the 2012 accretionary package and morphodynamic evolution of the point bar: the synthetic stratigraphy approach* section). In this phase, lidar data were processed for the removal of vegetation and for the reconstruction of the channel thalwegs, where data points were missing because of the presence of water during the scanning period (Fig. 3B). For the vegetation removal and to homogenise point density, the lowest point of the raw data for each pixel of

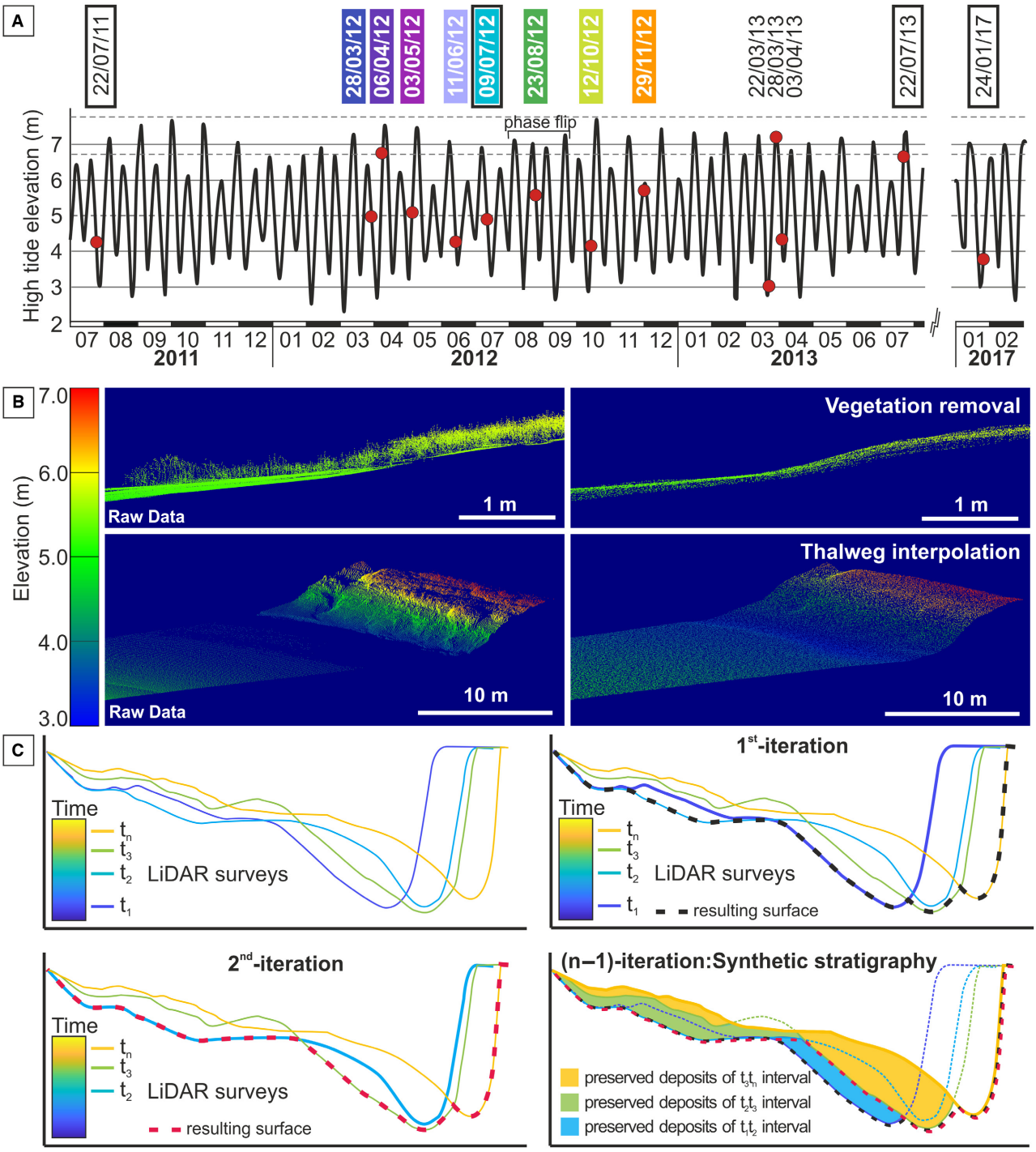

Fig. 3. Methodologies used to define and analyse the 2012 accretionary package. (A) Date of the lidar surveys between 2011 and 2017 relative to the high tide elevation. (B) Example of the raw data processing for the vegetation removal and for the reconstruction of the thalweg zone. (C) Simplified diagram showing the synthetic stratigraphy approach, which allows to define the effectively preserved accretionary units. See text for explanation.

20 cm grid was kept. Manual validation ensured that no vegetation points remained. This process is particularly effective where sparse patches of vegetation occur, whereas densely vegetated areas were not included in the following analyses (i.e. above 6.2 MAMSL) because the ground cannot be detected below vegetation. For the interpolation on the missing data of thalweg

zone due to stagnant low tide water (i.e. below 3.75–4.00 MAMSL), the grid of ground point cloud was transformed into a triangulated irregular network via the Poisson Surface Reconstruction algorithm (Kazhdan *et al.*, 2006; Kazhdan & Hoppe, 2013), as implemented in CloudCompare (set parameters: octree cell size of 0.0003 m, octree depth of 10 and radius of 3 m to compute the surface normal orientation). Using a multiscale approach and accounting for surface normal orientation, the Poisson Surface Reconstruction provided a visually realistic interpolation of the thalwegs. Because of this interpolation process of the channel thalweg, the authors do not quantitatively interpret this part of the results. The obtained surfaces are sampled at a regular grid (1 m resolution), and the resulting point clouds are used for the creation of the synthetic stratigraphy (see next section).

Identification of the 2012 accretionary package and morphodynamic evolution of the point bar: the synthetic stratigraphy approach

The synthetic stratigraphy approach allows one to superimpose multi-temporal topographic surfaces and identify the spatial distribution of the deposits accumulated in a defined time interval at the net of all the following erosional processes occurring in the area. Thus, this approach helps in understanding the morphodynamic evolution of the point bar in a precise time period. Multi-temporal topographic data have been widely used to create point-bar synthetic stratigraphy and assess patterns of erosion and deposition in laboratory experiments (Van de Lageweg *et al.*, 2013; Lentsch *et al.*, 2018). Nevertheless, this is one of the first attempts (Braat *et al.*, 2019) to integrate a synthetic-stratigraphic model with related real core data from a field case. In this research, the lidar data have been used to create a synthetic stratigraphy of the study point bar, in order to define the spatial distribution of the deposits forming the 2012 accretionary package, along with their internal architecture.

The synthetic stratigraphy was obtained by means of a Python™ script. Selecting from the oldest (1st-iteration) to the youngest (n-iteration) survey, each point cloud has been lowered wherever a younger survey shows a lower elevation (i.e. where erosion occurred). At the $(n-1)$-iteration the synthetic stratigraphy was created (Fig. 3C). Measuring the vertical distances between the obtained point clouds reflects the thickness of the preserved deposits in the point bar. This approach allowed the authors to discriminate seven preserved sub-volumes accreted between successive surveys (hereafter termed 'internal increments'). In order to provide a simple nomenclature of the increments, each one was named with the date of the older survey: for example, the internal increment of sediments deposited between 03 May 2012 and 11 June 2012 and preserved in the synthetic stratigraphy was named '03/05/12 internal increment'.

An estimation of the resulting volumes has been performed using a CloudCompare tool ('Compute 2.5 volume' which computes a vertical difference of digital elevation models interpolated from the point clouds and sums up the difference accounting also for pixel size). This procedure allowed identification of the overall volume of sediments forming the 2012 accretionary package.

Point-bar deposits: surface and core data

A detailed geomorphological investigation of the study point bar was performed in September 2017, in order to document surface sediment distribution and sedimentary processes (Fig. 5), whereas seven sedimentary cores were collected in June 2018. Cores were recovered along the point-bar brink (Fig. 2C) and coring sites were georeferenced using a differential GPS with a maximum position uncertainty of 6 cm. Coring aimed at picking up sediments along the point bar (landward and seaward sides) and, above all, at recovering deposits forming the 2012 accretionary package. Sedimentary cores, each up to 3.0 m deep, were recovered using an Eijkelkamp hand auger (Eijkelkamp Soil & Water, Giesbeek, The Netherlands) with a 1.0 m long gouge sampler which has a diameter of 30 mm. Core sediment samples were kept humid in PVC liners and then cut longitudinally, photographed and stored as sedimentary peels produced using epoxy resins. Cores were measured following basic principles of facies analyses to understand the overall distribution of sedimentary facies in different parts of the point bar (Fig. 5). Deposits from the 2012 accretionary package (Figs 6 and 7) were identified knowing the elevation of the surfaces bounding its base and top, which ranges between 4.09 and 5.28 MAMSL in the area where the cores were collected. A limitation on the detection of the 2012 accretionary

package can arise from an uncertainty in the vertical resolution, derived from: (i) precision of instruments on the elevation measurements; (ii) reshaping of the surveyed morphologies (for example, tidal bore events could form stratigraphic surfaces/boundaries which do not perfectly match the surveyed ones); and (iii) compaction of areas with a certain amount of muddy deposits. Considering the instrument precision, the limited occurrence of fine-grained sediments, and the lack of anomalous tide events, the authors estimate that such an uncertainty should not exceed 10 cm.

A quantitative classification of different sedimentary features of the cored deposits has been developed (Fig. 9). Each core has been subdivided into 1 cm thick intervals, and each interval has been characterized on the basis of: (i) percentage of sand and mud (i.e. comprising both silt and clay) fraction (five classes on the basis of the sand percentage: 100%, more than 60%, between 30% and 60%, less than 30%, and 0%); (ii) sedimentary structures (for example, cross-laminations, plane-parallel laminations); and (iii) occurrence of roots, oxidation, mud cracks and mud clasts. Pie charts have been created to summarize data on grain size and sedimentary structures of each core (Fig. 10). Grain-size data have also been plotted as pie charts for the different internal increments in order to investigate possible correlations between grain-size changes and tidal excursion (Fig. 8). Sedimentary structures have also been analysed on the lidar topographic surveys (Fig. 11) in order to better identify morphologies and orientation of ripple forms recorded at the end of the ebb phase (i.e. when the surveys were performed). The analysis can only be performed near the location of the instrument where point cloud density is large enough to detect bedform features and orientation. Vegetation removal and classic hill shade techniques, available in CloudCompare, have been used on the raw point clouds to better highlight these features.

In order to investigate preservation of the tidal signature in the 2012 accretionary package, attention has been paid to the rhythmic alternation of sandy and muddy laminae and progressive changes of related thickness (Figs 4 and 13). As firstly highlighted in the Bay of Mont-Saint-Michel by Tessier (1993), couplets of sandy/muddy laminae are accumulated during an elementary tidal cycle (TC), while progressive thickening and thinning of these laminae represents the semi-lunar tidal cycle, or neap/spring sequence (NS sequence). Preservation of TCs and NS sequences is strongly controlled by elevation (Tessier, 1993; Archer, 1998; Davis, 2012). The highest number of tidal couplets can potentially be preserved in the subtidal zone, where all of the ebb slack water can accumulate muddy laminae. In the subtidal zone, a TC is composed of two couplets of sandy/muddy laminae and a NS sequence (site 1, Fig. 4A), in semi-diurnal conditions, can be made up of 28 TCs (14 days). Moving upward from the subtidal zone (Fig. 4A), the number of couplets forming a tidal cycle decreases, and NS sequences will be formed by a reduced number of TCs (Tessier, 1993, 1998; Archer, 1998). In the upper-intertidal zone (site 4, Fig 4A), where flooding occurs only during the highest spring tides, the NS sequence will consist only of a limited number of TCs, which will contain only flood slack water mud drapes (Tessier, 1993). Tessier (1993) analysed tidal rhythmites in the upper-intertidal zone of the Sélune estuary in the bay of Mont-Saint-Michel and recorded NS sequences consisting of 10 to 12 TCs, out of the 28 possible in a semi-diurnal regime. Progressive changes in thickness of TCs can define different NS sequence trends (Fig. 4B), including: (i) thickening to thinning-upward trend (i.e. a thickening – thinning NS sequence); (ii) thickening or thinning-upward trend (i.e. a partial NS sequence); and (iii) no trend (i.e. absence of NS sequence). Pie charts have been created to summarize data on the occurrence of NS sequences of each core (Fig. 13).

Tide data sources

Tide data series for the study time interval (Fig. 3A) were supplied by the Service Hydrographique et Océanographique de la Marine (http://refmar.shom.fr). Tide elevation at Mont-Saint-Michel was transposed from the measurements of the nearest gauge located in Saint-Malo, *ca* 40 km west of the study area (Fig. 1A). According to Roux (1998) and confirmed by Leroux (2013), tide elevation in Mont-Saint-Michel is 5.7 m lower than that at Saint-Malo gauge. Tide data allowed the authors to establish how many times the studied channel was flooded either during spring or neap tides. Flooding frequency at different elevations has been calculated as the ratio between the number of tides reaching a specific elevation divided by the number of tides that occurred during the study period (i.e. between 28 March 2012 and 29 November 2012). The mean number of tides per

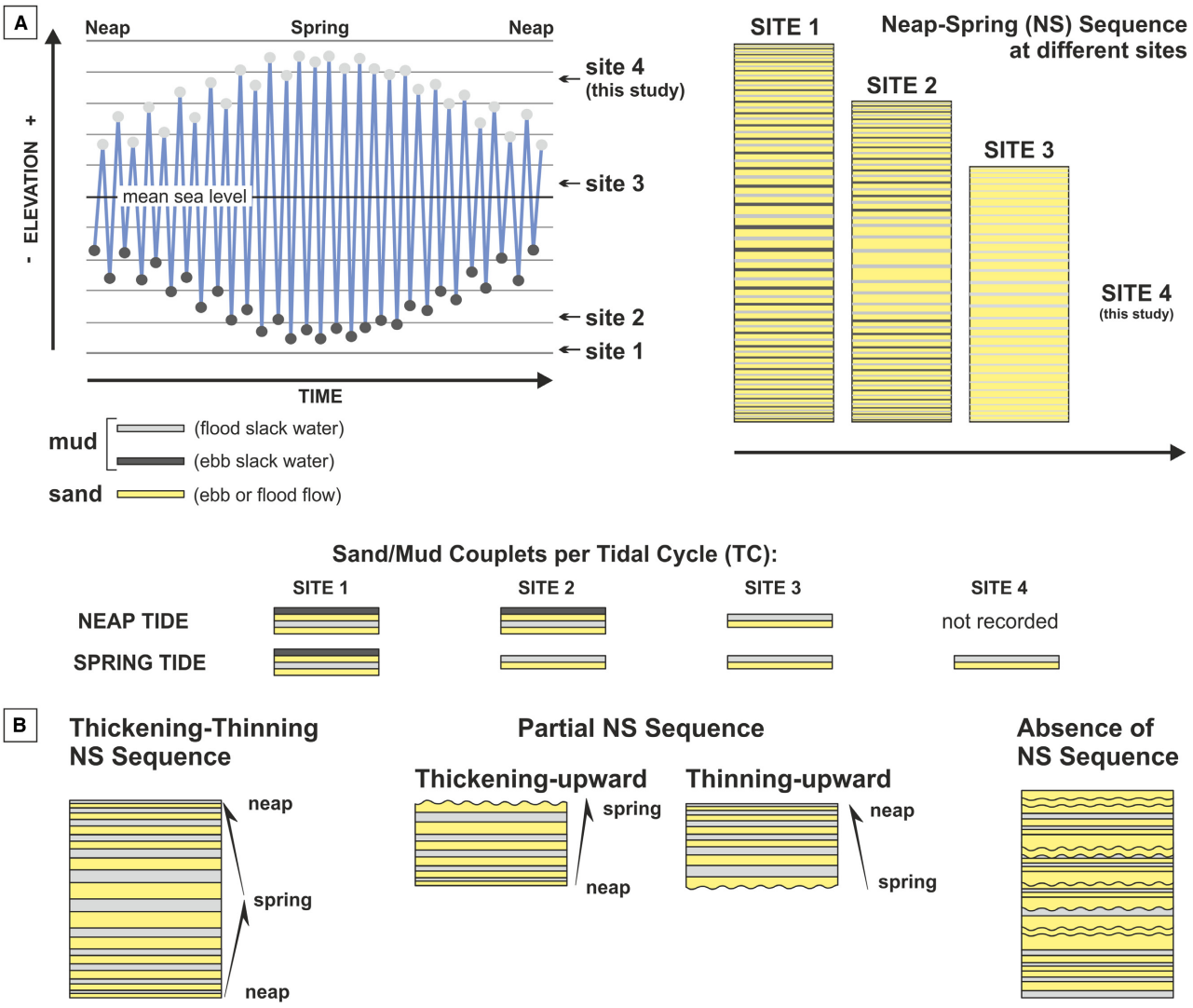

Fig. 4. (A) Idealized sketch illustrating deposits related to a Tidal Cycle (TC) and a neap–spring (NS) sequence at different elevations with respect to Mean Sea Level (MSL) and (B) criteria to define different amount of preservation for tidal rhythmites within a NS sequence in an upper intertidal setting.

neap–spring cycle at different elevations has been calculated as the mean between the number of tides of each neap–spring cycle that reached a specific elevation during the study period (Fig. 9).

RESULTS

Point-bar morphology and deposits

Different deposits were accumulated by specific depositional processes in three main zones of the studied bend: point-bar-top, point-bar-slope and channel-thalweg zones (Fig. 5). The elevation of these areas changes from *ca* 5.5 to 6.0 MAMSL of the point-bar top, to *ca* 4.1 to 3.5 MAMSL of the channel thalweg. This is reflected in the flooding frequency of these areas (Figs 5B and 7C): tides reaching the point-bar top (i.e. reaching the elevation of 5.5 MAMSL) are only 39% of the total (i.e. 182 out of 467 tides during the study period); whereas, the flooding frequency at the channel thalweg (i.e. at the elevation of 4.1 MAMSL) increases to 76% (i.e. 353 out of 467 tides during the study period).

The point-bar-top zone is characterized by a flat topography (Fig. 5A and B) and by the presence of a sparse vegetation cover (Fig. 5C). Point-bar-top deposits consist of plane-parallel laminated mud with silt and very-fine sand

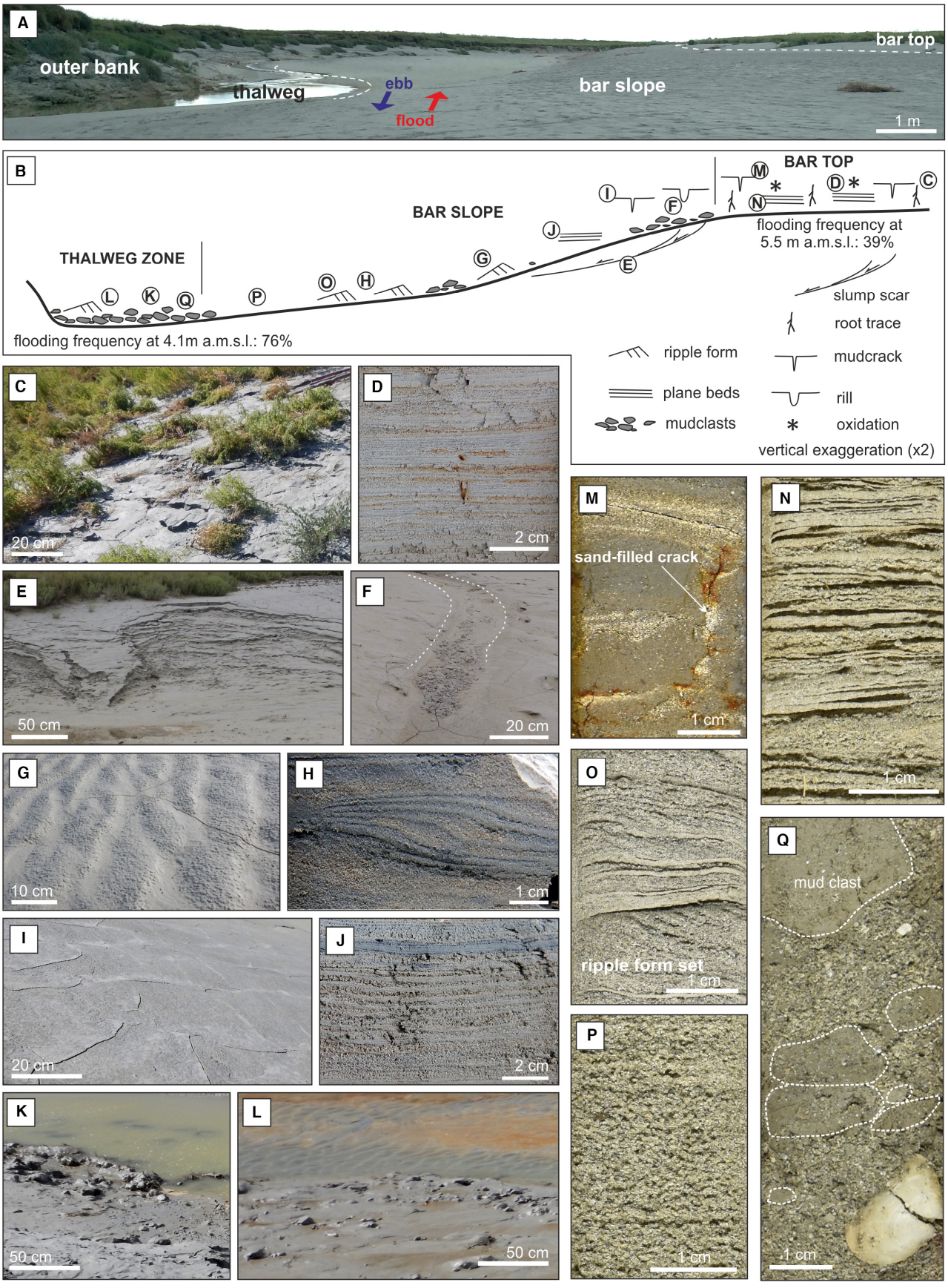

Fig. 5. Morphological and sedimentological features of the study site obtained from the 2017 field survey – (A) to (L) – and sedimentary cores – (M) to (Q). The axial zone of the study bend (A) and cross-sectional sketch (B) showing spatial distribution of different sedimentary features. (C) Sporadically vegetated point-bar top. (D) Plane-parallel laminated and oxidized point-bar top deposits showing clear tidal couplets. (E) Bank collapses affecting the landward side of the point bar. (F) Mud clasts at the outlet of a minor rill cut in the upper part of the point bar. (G) Current-ripple forms in the central part of the point-bar slope with rain droplet craters. (H) Rhythmic lamination within a climbing-ripple form. (I) Mud cracks in the upper part of the point-bar slope. (J) Rhythmic lamination in plane-parallel laminated point-bar deposits accumulated in the upper slope. (K) Cobble to pebble-sized mud clasts in the channel thalweg zone, where current ripples develop (L). (M) Point-bar top mud showing a sand-filled desiccation fracture. (N) Plane-parallel stratified sand with muddy laminae developed during slack water stages. (O) Ripple cross-laminated sand with mud drapes. (P) Mud-free fine sand from the lowermost part of the point bar. (Q) Channel lag medium sand with scattered mud clasts and shell fragments.

concentrated in 1 to 2 mm thick laminae (Fig. 5D). Polygonal mud cracks are common in this zone, and they are often filled with sand (Fig. 5M). Oxidation due to prolonged subaerial exposure commonly occurs (Fig. 5D).

The point-bar slope connects the point-bar-top with the channel-thalweg zone, and dips up to 20°. Inclination decreases from the upper (10 to 15°) to the lower (5 to 10°) slope (Fig. 5A and B). Point-bar slope is characterized by current ripple and plane beds (Fig. 5G, H and J), polygonal mud cracks (Fig. 5I), rills and local accumulation of flat mud clasts (Fig. 5F). Slumps commonly occur in this zone (Fig. 5E). The related deposits consist of sediments ranging in grain size between mud and fine sand. These deposits are plane-parallel and ripple cross-laminated, and laminations are commonly marked by muddy laminae (Fig. 5N and O). Moving from the upper to the lower point-bar slope, sand content increases and muddy laminae become progressively less common (Fig. 5P).

The channel-thalweg zone shows an irregular topography (Fig. 5A, B, K and L). Mud clasts are spherical, and are up to 10 to 15 cm in size (Fig. 5K). They occur individually or in clusters over a sandy bed, which contains shell fragments and is locally characterized by current ripples. Channel-thalweg deposits are mainly massive (Fig. 5Q) and characterized by mud clasts and shell fragments.

The 2012 accretionary package

Synthetic stratigraphy

Synthetic stratigraphy shows that the 2012 accretionary package consists of *ca* 3300 m^3 of deposits, which were accumulated mainly in the point-bar-slope zone (Fig. 6). The substrate of the 2012 accretionary package sloped from the point-bar-top (*ca* 5.5 to 6.0 MAMSL) to the channel-thalweg zone (*ca* 3.75 MAMSL) (Fig. 7). The 2012 accretionary package forms an arcuate sedimentary body, that follows the pre-existing point-bar morphology. This sedimentary body pinches out towards the point-bar top and channel thalweg (Figs 6 and 7C). A cross-section along the point-bar axis (Fig. 7A and C), shows that it is *ca* 20 cm thick in the point-bar-top zone, with single internal increments (i.e. preserved sub-volumes accreted between successive surveys) of few centimetres (Fig 7C). In contrast, few deposits accumulated in the thalweg zone, with evident cross-cutting relationships between the different internal increments (Fig. 7C). Thicker deposits are recorded on the point-bar-slope zone (Fig. 7C) and they form a rim along the whole point bar (Fig. 6). The maximum thickness is *ca* 1 m (Fig. 6) and is recorded in the bend-apex zone (i.e. cores 2 and 3), although 70 cm thick deposits occur along the landward side of the accretionary package (cores 0 and 1). An along-bend cross-section (Fig. 7B and D) shows that the 2012 accretionary package thins towards the seaward side of the point bar, whereas along the landward side it is abruptly cut (Fig. 7D) by a secondary tributary channel (Fig. 1).

The analysis of the spatial distribution of these increments suggests that the overall expansion of the point bar (Fig. 2B and C) was achieved by a non-uniform storage of sediments along the inner bank of the bend (Figs 7D and 8A). These localized accretionary episodes affected different parts of the point bar (Fig. 8A) including: (i) the seaward side ('12/10/12 internal increment'); (ii) the landward side ('09/07/12 internal increment'); (iii) both the landward and seaward sides ('03/05/12, 11/06/12 and 23/08/12 internal increments'); and (iv) the point-bar-apex zone ('03/05/12, 11/06/12, 09/07/12, 23/08/12 and 12/10/12 internal increments'). The analysis of the channel thalweg dynamic during the study period (Fig. 8A) shows that in the point-bar-apex zone and in the landward

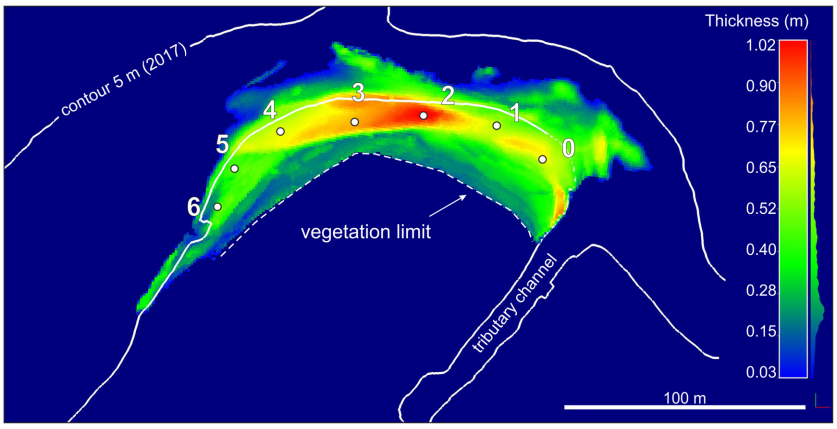

Fig. 6. Thickness distribution within the 2012 accretionary package. Positions of the study cores and contour related to 5 m elevation of 2017 survey are also shown.

side, the channel thalweg was quite stable. Whereas, in the seaward side, ebb and flood flows induced a bifurcation of the thalweg zone, that followed back and forth movements in an east–west direction. Along the seaward side, eastward shift of the flood thalweg caused the creation of a local accommodation space, which was filled with sediments during the following westward shift (for example, '12/10/12 internal increment'). In the point-bar-apex zone, the '03/05/12 internal increment' also shows a major scour depression (i.e. concave-upward surface), that was filled up during following accretionary stages (Fig. 7D).

Preservation of internal increments changes along the bend. Preservation is highest in the point-bar-apex zone, where five increments (03/05/12, 11/06/12, 09/07/12, 23/08/12 and 12/10/12 internal increments') are preserved. Whereas, the lowest preservation occurs along the seaward side of the point bar, where only two or three increments are recorded.

Sedimentology

Grain size varies both vertically and laterally within the 2012 accretionary package (Fig. 9). Specifically, sand content increases both downbar and seaward within the accretionary package (Fig. 10B). The lowest sand content occurs in the central-point-bar zone (cores 1 to 3), where the accretionary package reaches its maximum thickness, and the minimum amount of sand is in core 1, just landward of the bend apex (Fig. 10B). In this core, the highest amount of mud is also recorded (with the 0% sand class representing 7% of the core thickness). Abundance of mud is registered in the central-point-bar zone (cores 1 to 3), where grain-size classes with less than 60% of sand (i.e. higher mud content) represent 38 to 78% of the accretionary-package thickness. Accretionary deposits along the seaward side of the point bar (i.e. cores 4 to 6) are characterized by the lowest amount of mud: grain-size classes with less than 60% sand representing between 5% and 36% of the accretionary-package thickness, and the 0% sand class (i.e. 100% mud) is registered only in core 6 (Fig. 10B) and consists of pebble-sized intraclasts. These mud clasts are locally oxidized and contain plant debris, suggesting that they were sourced through collapses from either the upper-point-bar zone or the outer bank. In most of the cores, mud clasts are scattered and millimetric in size. They show both rounded or flat shapes, and are commonly oriented according to the main stratification.

Sedimentary structures in the 2012 accretionary package consist of plane-parallel stratification and current ripple cross-laminations (Fig. 9), and their spatial distribution does not show any specific trend, neither vertically nor along the bend in the collected cores (Fig. 10B). Spatial distribution of bedforms along the point-bar surface (Fig. 11) at the end of the ebb-phase shows that along the landward (Fig. 11H) and seaward (Fig. 11B) sides, the point-bar surface is quite flat (Fig. 11B), with localized development of current ripples (Fig. 11H), which are usually flood-oriented in the seaward side and ebb-oriented in the landward side (Fig. 11H). In the apex-zone, both flood-oriented (Fig. 11F) and ebb-oriented (Fig. 11G) current ripples occur in separated areas, close to one another (Fig. 11C) and nearby the vegetation limit. Much more complex 3D current ripples occur towards the main channel, whose orientations are not straightforward (Fig. 11E). Deposits accumulated on the point-bar slope also show local evidence of deformation (Fig. 10B), which could be ascribed to gravitational collapses or tidal bore

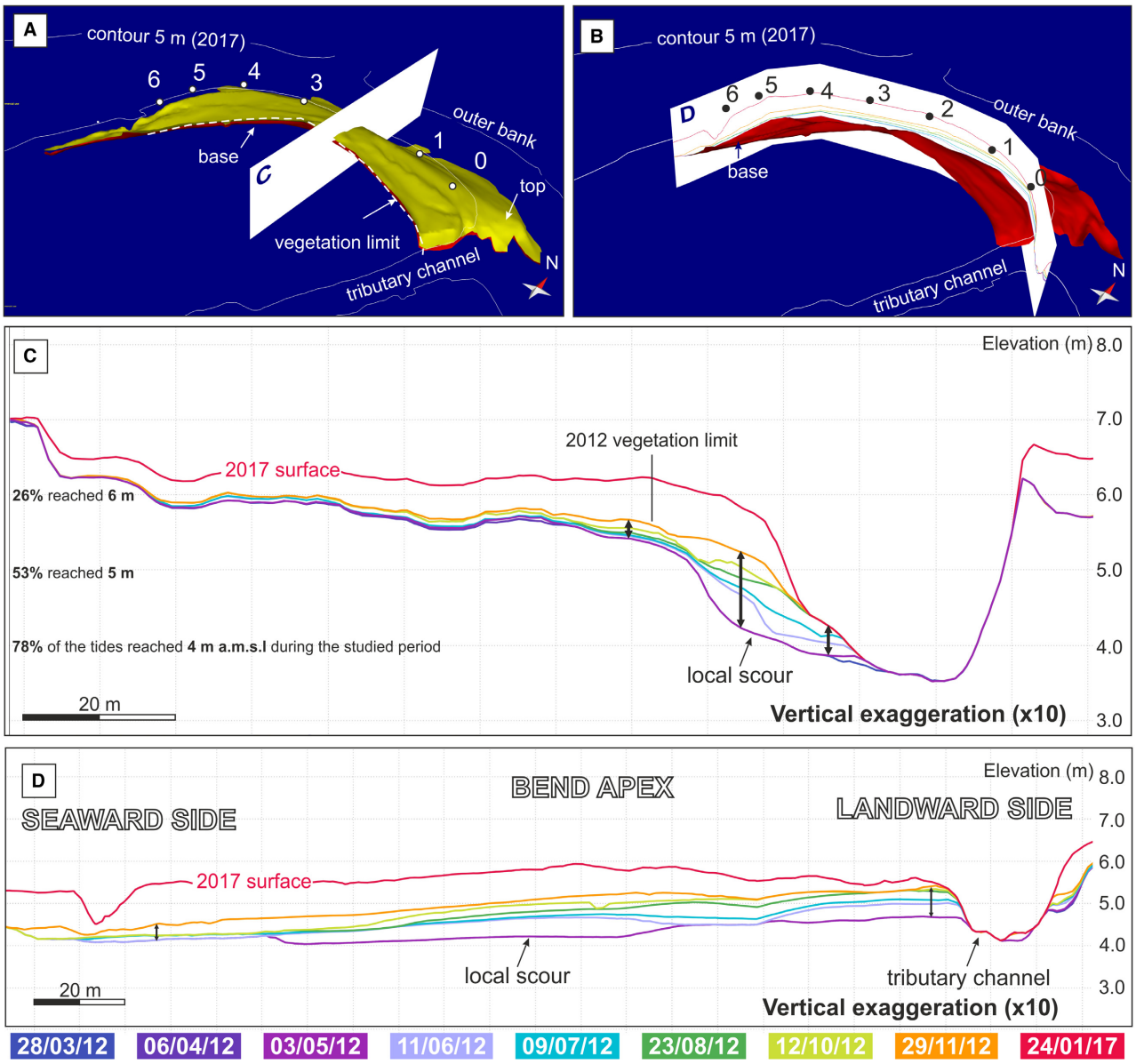

Fig. 7. Synthetic stratigraphy of the 2012 accretionary package. (A) and (B) Location of a cross-section cutting the accretionary package along the bend axis (A) and along the 2017 point-bar brink (B). Position of the study cores is also shown. Axial (C) and along-bend (D) cross-sections showing the internal increments within the study accretionary package. Dark-grey arrows indicate 2012 accretionary package thickness variations.

related deposits, although the limited diameter of cores prevents observations at higher resolution.

Integration between synthetic stratigraphy and grain-size data (Fig. 8) shows that the smallest amount of clean sand (i.e. 25%) occurs in '09/07/12 and 23/08/12 internal increments' (Fig. 8B), which accumulated when sediment was mainly stored along the apex and landward side of the point bar (Fig. 8A).

Tidal signature in the 2012 accretionary package was analysed to quantify the spatial distribution of thickening – thinning or partial NS sequences (Figs 4 and 9). A thickening – thinning NS sequence (Fig. 12) can vary in thickness between 1 cm (i.e. condensed sequences) and 7 cm (i.e. expanded sequences), and can be made up of nine to twelve TCs. A single tidal couplet, representing one tidal cycle (i.e. one TC), consists of a sand laminae overlaid by a mud laminae. It is commonly only a few millimetres thick, but its thickness can range from 1 mm to 1.5 cm in condensed and

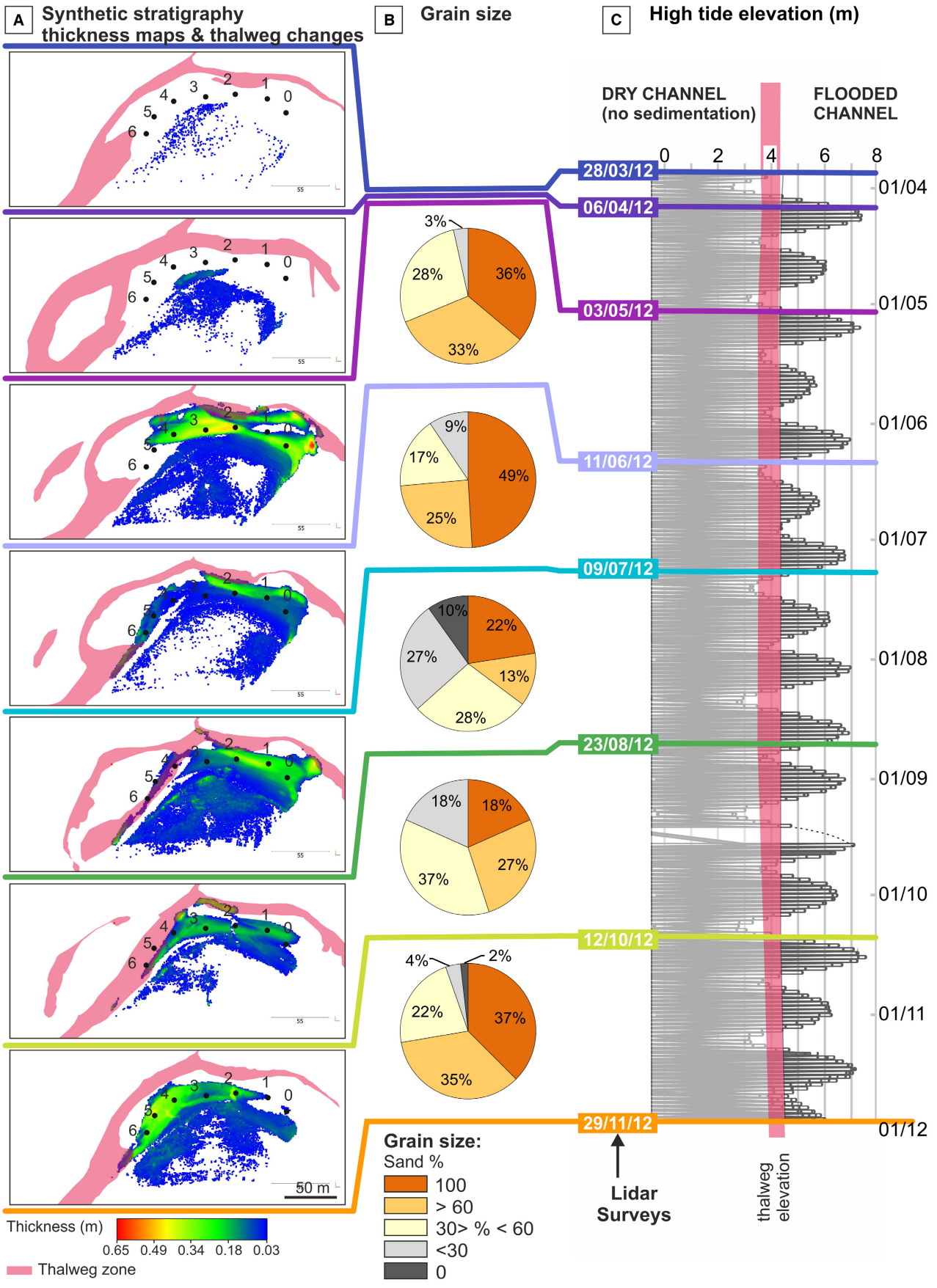

Fig. 8. Point-bar sedimentation and channel thalweg displacement during accumulation of the 2012 accretionary package. Sediment thickness and channel thalweg displacement (A), grain-size distribution (B), and tide elevation (C) during formation of the seven accretionary increments. In (A), channel thalweg position during the younger survey is showed, highlighting temporal displacement of the thalweg. In (C), note that only a limited number of tides carried water at an elevation higher than the channel thalweg (in red).

expanded sequences, respectively (Fig 12). Expanded sequences commonly contain abundant sand, whereas condensed sequences can be either mud-rich or sand-rich (Fig. 12). The number of TCs forming a thickening – thinning NS sequence roughly decreases from twelve to six going from the base to the top of the 2012 accretionary package. At these elevations, the mean number of tides forming a neap–spring cycle is 21.9 (measured at 4.1 MAMSL) and 13.6 (measured at 5.3 MAMSL), respectively (Fig. 9). Abundance of thickening – thinning NS sequences varies along the bend (Fig. 13) from 0 to 26% of the 2012 accretionary package thickness. They are more common (i.e. >10% of 2012 accretionary package thickness) in the central-point-bar zone (i.e. cores 1 to 4) and reach the maximum abundance in core 1 (i.e. immediately landward of the bend apex). In cores 1 to 4, NS sequences are not distributed at any specific elevation, and can occur randomly in the accretionary package (for example, cores 1 and 3), or in its higher (for example, core 2) or lower portion, within the infill of the scour depression (for example, core 4). Partial NS sequences are spatially distributed along the bend and represent 5 to 18% of the accretionary package thickness of interest, except for core 6 (i.e. the most seaward core), where neither thickening – thinning nor partial NS sequences are recorded (Fig. 13). Partial NS sequences are commonly associated with or located in close proximity to thickening – thinning ones. As a whole, the spatial distribution of thickening – thinning and partial NS sequences show that tidal signal on sedimentation is mainly preserved in the central-point-bar zone, where rhythmites (i.e. thickening – thinning and partial NS sequences) occur at different elevations and form up to 40% of the 2012 accretionary package.

DISCUSSION

Point-bar growth and sediment distribution

The yearly lidar-survey analysis, focusing on the short-term evolution of the point bar, shows that planform changes of the study channel bend caused the bend apex to move away from the belt axis (Fig. 2B and C), pointing to an overall expansion of the point bar and to an increase of channel sinuosity. Although this would fit with classical morphodynamic models for tidal point bars (Bridges & Leeder, 1976; De Mowbray, 1983), comparison between different surveys and reconstructed synthetic stratigraphy highlights that increasing bend sinuosity is not achieved through a progressive bend expansion, but by alternating storage of sediments along the landward and seaward sides of the point bar (Fig. 8A). This morphodynamic evolution might reflect the presence of ebb and flood currents, which alternately dominated different portions of the bend promoting accretion along different sides of the point bar (Fig. 14). The complex interaction between point-bar morphology, tidal asymmetry and mutually evasive nature of flood and ebb flows causes: (i) inequalities between flood and ebb magnitude velocities and flow periods; and (ii) the spatial offset of the highest velocities, which act in different directions and at different magnitudes along the meander. In the study meander, the flood tide generally overtops the lower marsh and flows across the point-bar top, reaching the highest velocities in the seaward side of the meander; whereas the ebb tide generally flows alongside the channel, reaching the highest velocities near the outer bank, when the lower marsh has dried out and the water discharge is concentrated in the main channel (Figs 2E, 2F and 14). This flow configuration, in turn, impacts the distribution of erosional and depositional processes along the meander, resulting in the registered alternating accretionary behaviour. Other processes contributing to this behaviour of the study meander could be ascribed to: (i) local movement of the channel thalweg (Fig. 8A); and (ii) influence of the two tributary channels occurring on both sides of the study bend (Fig 1). The back and forth movements of the channel thalwegs in the seaward side of the meander cause the creation of a local accommodation space, which can be filled with sediments later on. This influence is quite clear considering the '12/10/12 internal

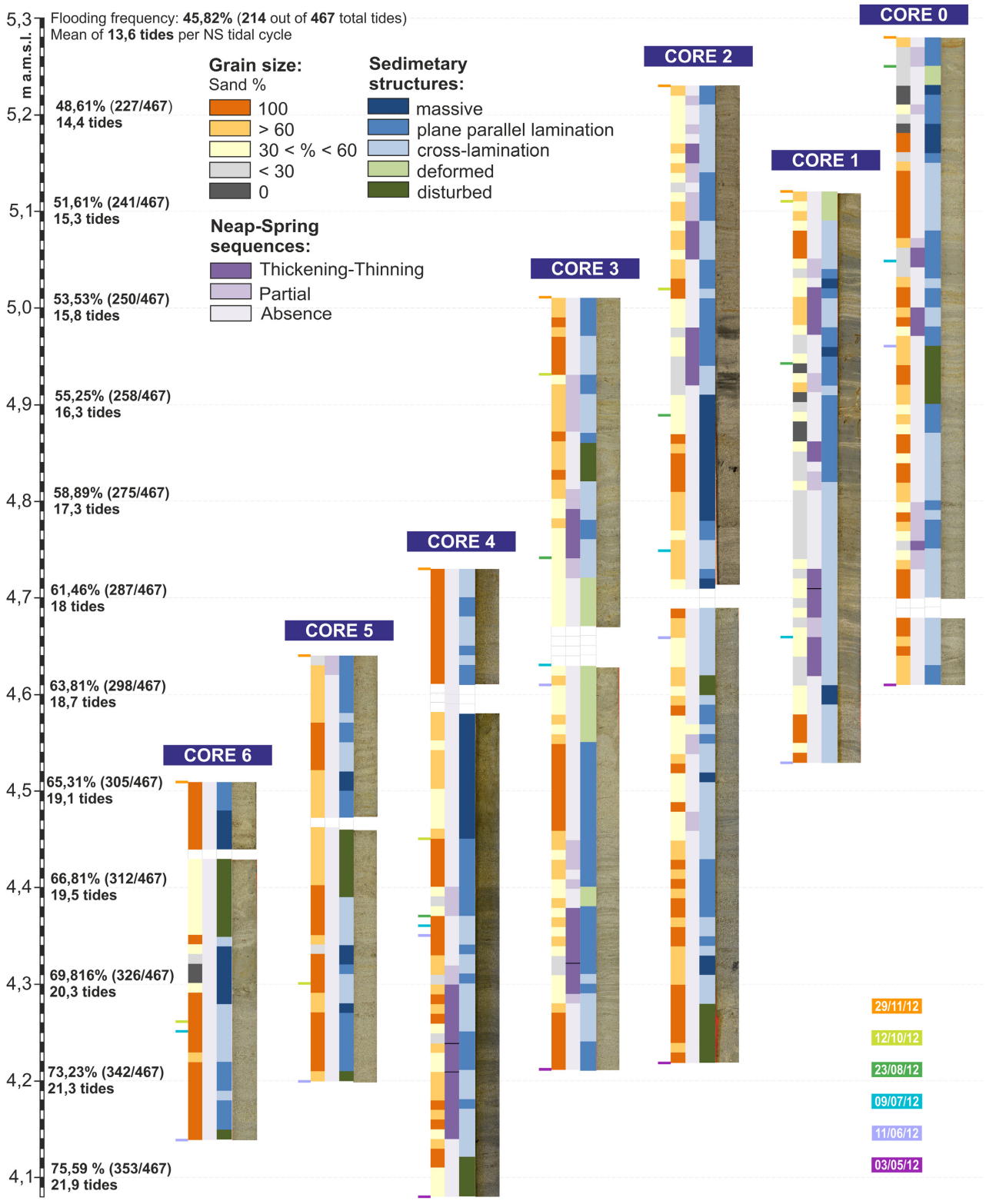

Fig. 9. Panel with the sedimentary cores collected along the point bar. Grain size, sedimentary structures, neap–spring (NS) sequence distribution and photographs of the cores are shown. The flooding frequencies and the mean number of tides per neap–spring cycle are displayed for different elevations.

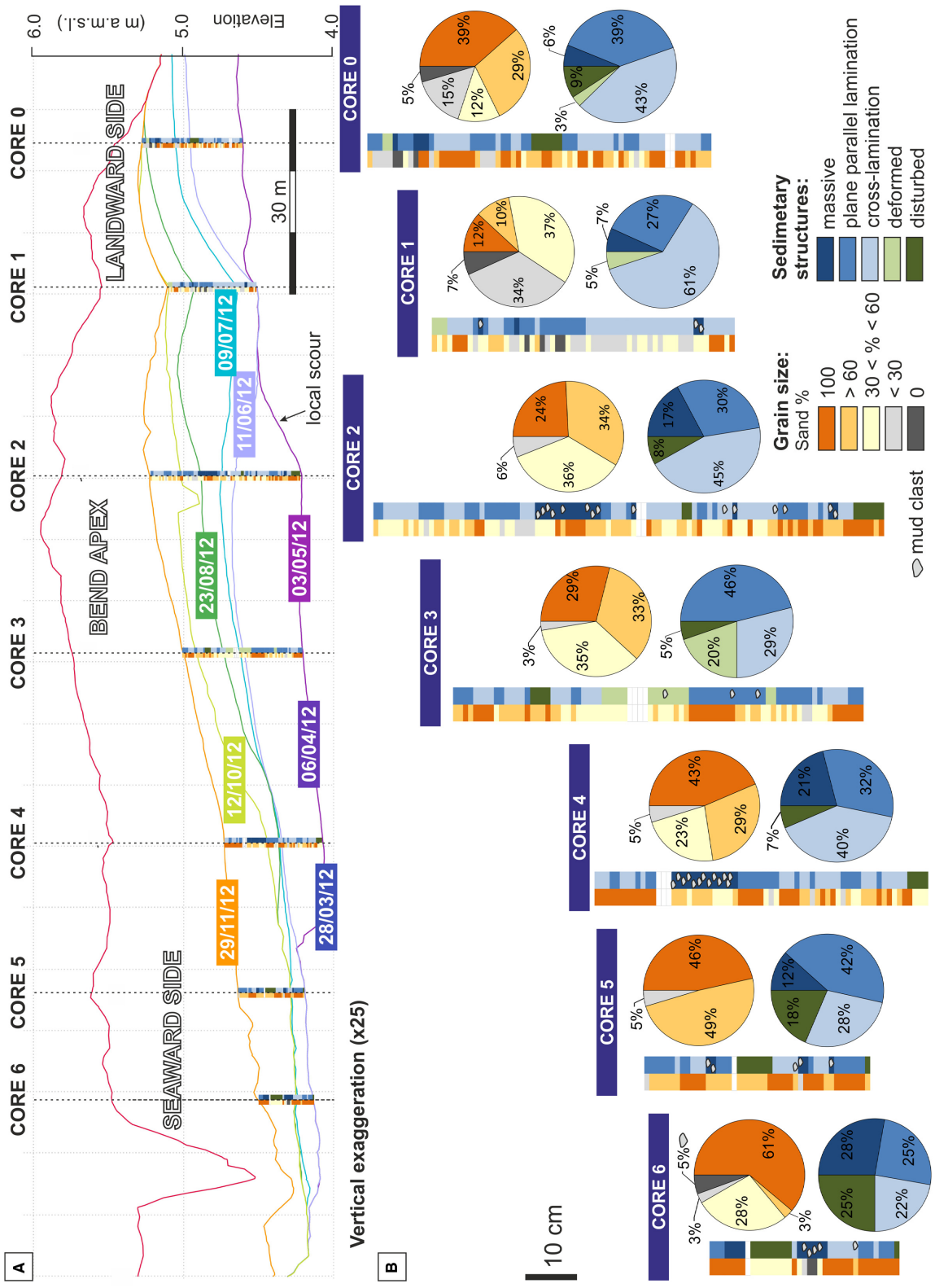

Fig. 10. Along-bend distribution of grain size and sedimentary structures within the 2012 accretionary package. (A) Location of the study cores along the bend and synthetic stratigraphy of the 2012 accretionary package. (B) Anatomy of the 2012 accretionary package. Pie charts show distribution of grain size and sedimentary structures for different cores based on samples of 1 cm intervals.

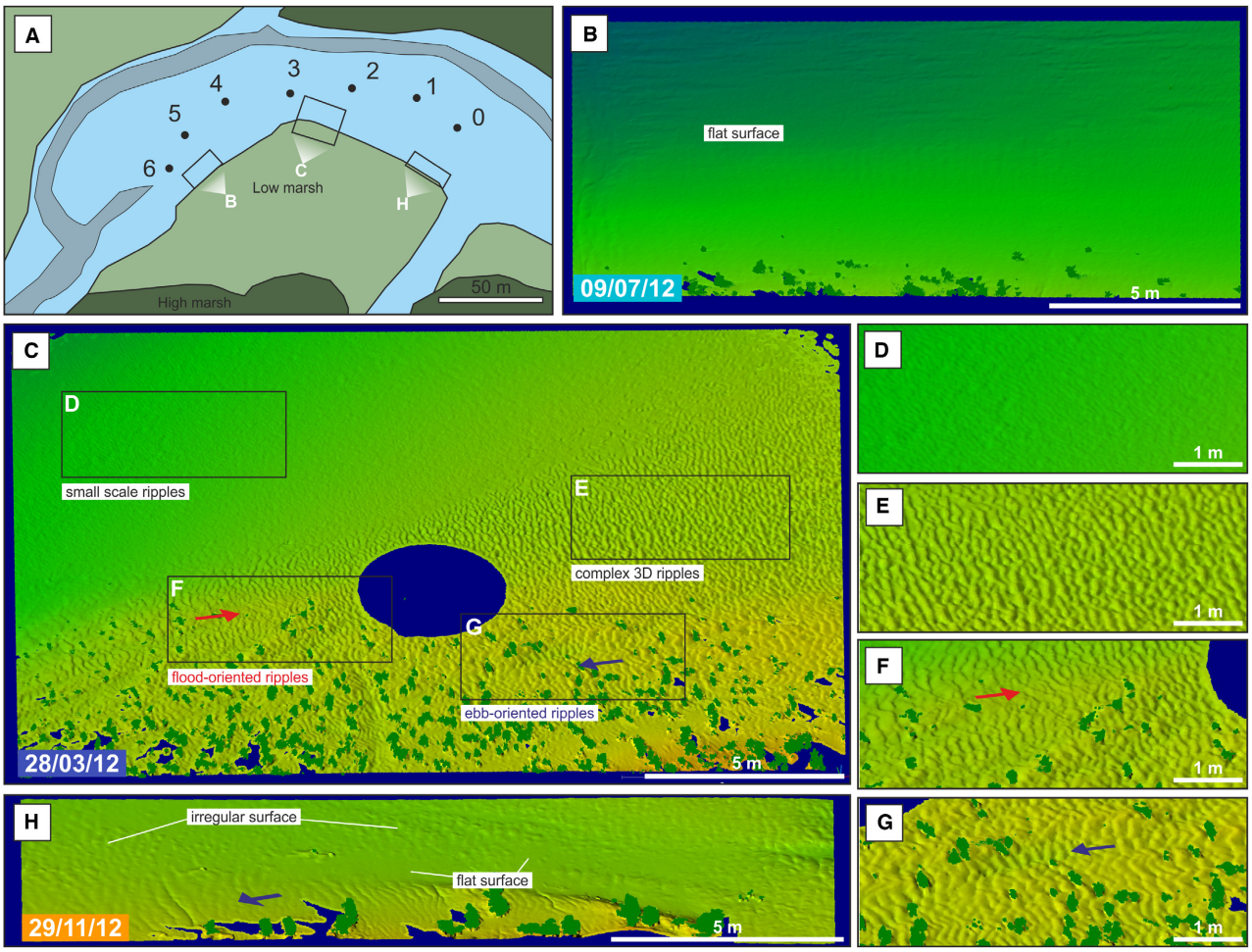

Fig. 11. Bedforms occurring along the point-bar surface in the studied period. (A) Location of the insets along the meander ('B', 'C' and 'H' labels indicate the point of view, numbers indicate core positions) (B) The seaward side of the point bar usually shows a flat topography and occasionally some asymmetric flood-oriented current ripples. (C) to (G) At the bend apex, small-scale ripples (D), complex 3D ripples (E), flood-oriented (F) and ebb-oriented (G) current ripples coexist in a limited area. (H) The landward side of the point bar usually shows a flat or slightly irregular topography, and occasionally some asymmetrical ebb-oriented current ripples.

increment': the thalweg was positioned in an eastward position during the '12/10/12 lidar survey' and later on it shifted towards the west ('12/11/29 lidar survey') leaving space for sediment accretion (Fig. 8A). It is not possible to assess the influence of the two tributaries on the point bar behaviour with the collected data. However, it is plausible that they play a role in enhancing erosion of the outer bank in different areas, particularly towards the north-east and towards the west for the landward and seaward channels, respectively. This in turn might influence the overall migration of the meander and growth of the point bar towards north-east and west, respectively.

The overall seaward migration of the point bar in the long-term scale (i.e. decennial timescale) was achieved through repeated landward and seaward shifts of the point bar occurring at a shorter timescale (i.e. few years) (Figs 2A and 14). Even though other analyses would be needed to further investigate the long-term behaviour, the overall seaward migration could be related to an ebb tidal dominance, a frequent phenomenon in tidal meanders (for example, the Western Scheldt); whereas the alternating multi-annual behaviour might point to the variation of ebb and flood dominance during higher order tidal cyclicality (for example, four-year tidal cycle). Furthermore, at the long-term scale, it seems that the progressive colonization by vegetation of the point-bar top, started in 2009 (Fig. 1B, C and D), corresponds to a period in

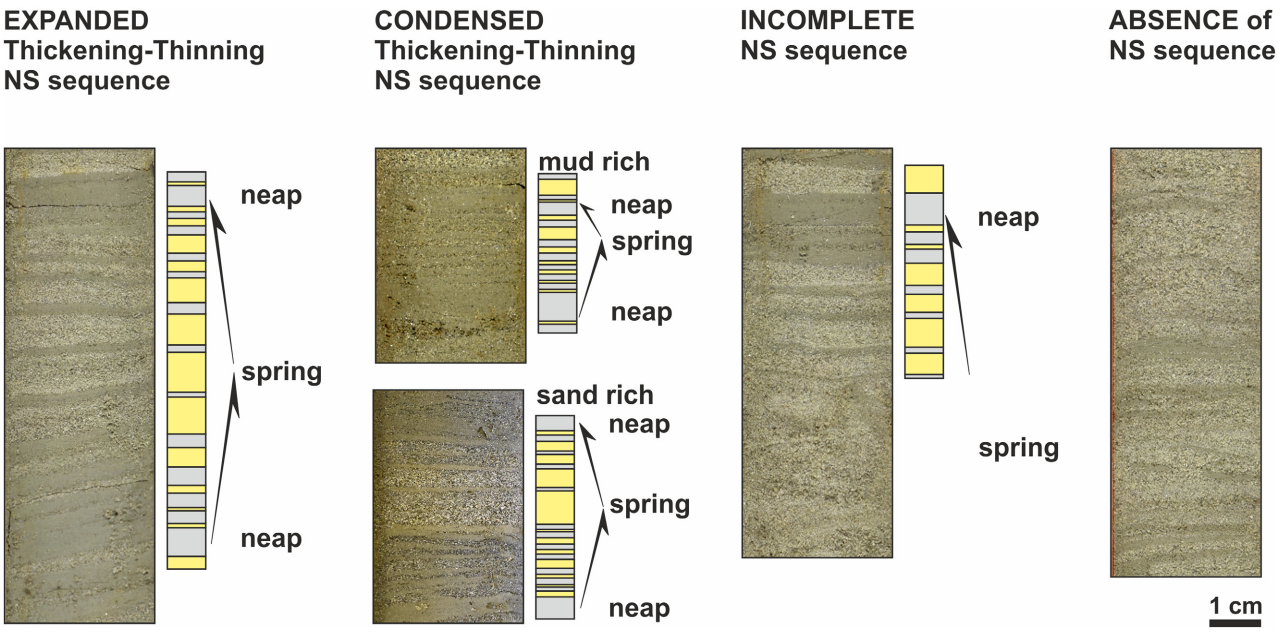

Fig. 12. Different expression of rhythmites within the 2012 accretionary package.

which the planform evolution of the meander changed from a predominant translation (with an overall seaward component) to a more expansional behaviour (Figs 2A and 14). This might be related to the increasing resistance of the sediments due to vegetation growth, which might have hindered the seaward migration and promoted an expansion. The occurrence of the thickest deposits in the point-bar-apex zone (Figs 6 and 7D) suggests that accumulation and preservation of deposits are more pronounced here than anywhere else along the point bar. This trend is confirmed by a comparison between 2012 and 2017 lidar surveys, that highlights the thickest deposits to occur repeatedly in the point-bar-apex zone (Fig. 7D). Sediment storage and preservation in this area can be explained by the flow configuration within a meandering channel. In a channel bend the main streamflow is forced towards the outer bank by the centrifugal force induced by the bend curvature, leading to the formation of a helical circulation. In the apex zone, and just downstream of it, maximum velocities are recorded along the outer bank, while a low-energy zone (i.e. shadow zone) develops along the inner bend. In sharp bends under certain hydrodynamic conditions, as demonstrated by Leeder & Bridges (1975), this area is characterized by flow separation and recirculation eddies, leading to stagnant water with a weak reverse flow. Although further field measurements would be required to demonstrate development of recirculation eddies in the study bend, the occurrence of low-energy conditions in the shade of the bend apex zone, especially during ebb flow of overmarsh tides (Fig. 2F), can explain the enhanced deposition (Leeder & Bridges, 1975; Riley & Taylor, 1978; Woodyer *et al.*, 1979; Thoms & Sheldon, 1996; Changxing *et al.*, 1999; Ferguson *et al.*, 2003), explaining the maximum thickness of the study deposits (Fig. 14). Occurrence of such a shadow zone also explains the paucity of clean sand in the point-bar-apex zone (cores 1 to 3 in Fig. 10), where mud settling was promoted by cyclically recurrent low-energy conditions. In this frame, mud accumulation also appears to be enhanced when subsequent spring tides show a similar amplitude (for example, '09/07/12 and 23/08/12 internal increments', and related tide elevation – Fig. 8). Similar abundance of mud in tidal rhythmites deposited during phase flip periods (i.e. periods in which spring tides show similar amplitude as an effect of the anomalistic month – Kvale, 2012), are visible in a macrotidal estuarine channel of the Gomso Bay, in the west coast of Korea (Choi, 2011, fig. 8), in the Miocene Marine Molasse Formation, Digne Foreland Basin, France (Couëffé *et al.*, 2004, fig. 6), and in the Mississippian Tar Springs Formation, Indiana, USA (Kvale, 2012, fig. 1.5c). Such mud abundance might be related to the fact that spring tides during phase flip periods show on average smaller tidal

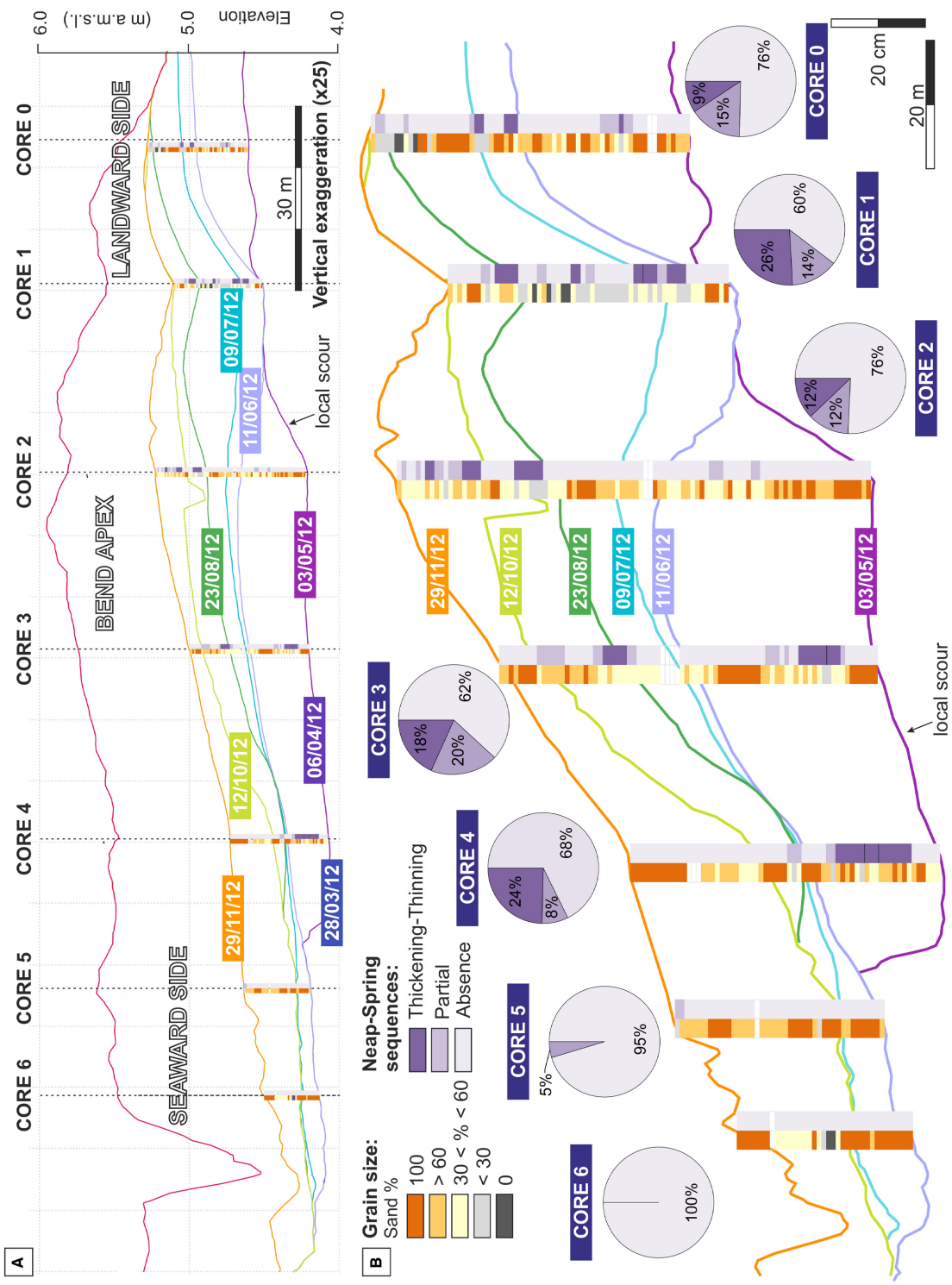

Fig. 13. Along-bend distribution of rhythmites and grain size within the 2012 accretionary package. (A) Location of the study cores along the bend. Synthetic stratigraphy of the 2012 accretionary package is shown along with distribution of grain size and sediments bearing different amount of rhythmites. (B) Anatomy of the 2012 accretionary package. Distribution of deposits recording thickening – thinning and partial neap–spring (NS) sequences is shown by pie charts.

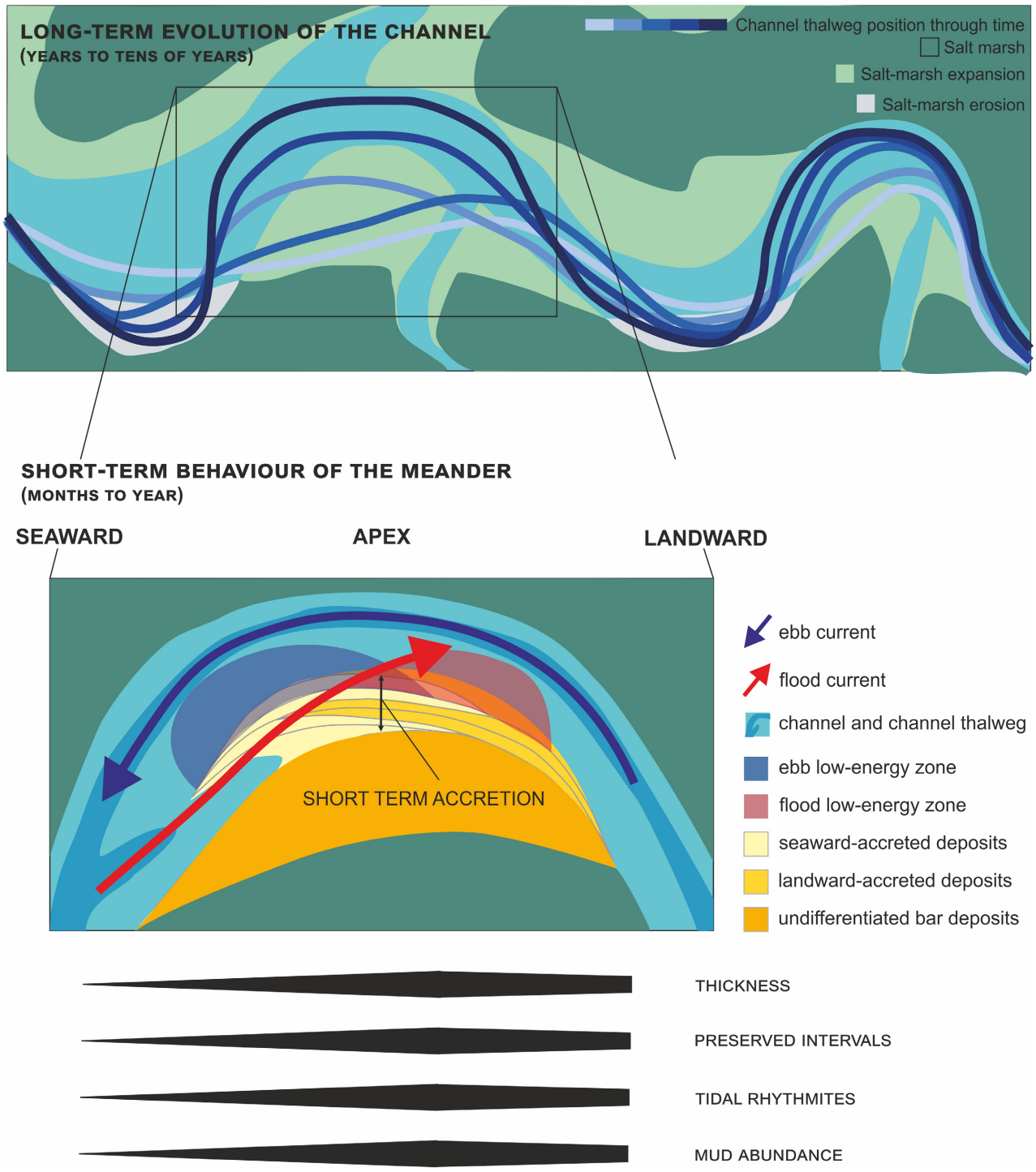

Fig. 14. Conceptual model showing the long-term and short-term evolution of the studied meander, highlighting the role of short-term dynamics and flow configuration in distributing sediments and preserving tidal signature along the point bar.

amplitudes, thus they are more favourable for mud deposition and preservation.

Mud-free sand is more common along the seaward and landward sides of the point bar (cores 0, 5 and 6 in Fig. 10), where high-flow velocity occurs on the point bar during flood and ebb stages, respectively (Leroux, 2013). In this frame, the occurrence of large amounts of clean sand

(>40%) with large mud clasts along the seaward side of the point bar (cores 5 and 6, Fig. 10B), suggests that flood currents strongly shape these areas, removing most of the mud drapes accumulated during slack-water stages. The reduced thickness of the 2012 accretionary package in this area fits with the dominance of erosion/bypass processes. The intensity of flood currents along the seaward side of the point bar, fits with substantial mud accumulation just landward of the point-bar apex, where the flood-related low-energy zone develops (cores 1 and 2, Fig. 10B). Although the strongest currents are recorded during the ebb phase of overmarsh tides (Fig. 2F), it arises that net point-bar sedimentation is mainly controlled by flood flows. Such a counterintuitive relationship (cf. Dalrymple & Choi, 2007) has also been highlighted by Choi *et al.* (2004) in a tidal point bar of the Han River Delta (Korea), where the mutually evasive nature of the ebb and flood current pathways causes the point-bar surface to be flood dominated, even though the channel as a whole is ebb dominated. Similarly, Ghinassi *et al.* (2018b) described an ebb-dominated translating tidal point bar in the Venice Lagoon (Italy), where sedimentation is mainly ascribed to flood flows.

Preservation of the tidal signal

As already highlighted by Tessier (1993, 1998) for tidal deposits of the Mont-Saint-Michel Bay, the elevation of the depositional site in comparison with the tidal range plays a key role in the number of tidal couplets forming a tidal sequence. Being placed in the upper-intertidal zone, the channel does not experience the ebb slack waters (Fig. 8C), and a tidal cycle (i.e. TC) is recorded by one couplet of sandy/muddy laminae. Additionally, tides hardly reach the channel during neap periods (Fig. 8C), meaning that the neap/spring cycles are formed by *ca* 22 tides at best (measured at the channel thalweg at 4.1 MAMSL), out of the 28 possible in a semi-diurnal regime (Fig. 9). The number of tides reaching the point bar progressively decreases towards the point-bar top (Fig. 9), where a neap–spring cycle is made up of 13.6 tides in mean (measured at 5.3 MAMSL). This is reflected in the number of TCs forming a NS sequence which decreases from 12 at the bottom, to six at the top of the 2012 accretionary package. Even though a lot of variability in the number of TCs per NS sequence is documented, these data would suggest that roughly half of the tides reaching the site are recorded in the tidal rhythmites.

The limited occurrence of NS sequences, either thickening – thinning or partial, indicates that formation and preservation of the cyclic tidal signal is not straightforward in such a dynamic upper-intertidal environment, although tides are the only effective forcing on sedimentation. Conditions needed for the formation and preservation of tidal rhythmites include: (i) a protected environment, which helps the expression of the regular variation of the tidal energy and avoids wave erosion; and (ii) a high suspended sediment concentration, which is needed for the creation of significant deposits for each tide and helps its preservation (Tessier, 1993; Davis, 2012). Therefore, tidal rhythmites are considered to be formed during and after a stage of offshore wave dynamics which favours sediment resuspension, and to be well-expressed in meandering tidal channels, since their morphology provides good protection from wave reworking (Tessier, 1993; Choi, 2011). Furthermore, in the upper intertidal domain, tidal rhythmite formation is considered to be promoted by tidal bore passage, which increases the suspended sediment concentration and produces tidal rhythmites thicker than normal (Furgerot *et al.*, 2013; Tessier *et al.*, 2017). Within tidal channels, preservation of the tidal signal is commonly discussed as a function of elevation (Choi *et al.*, 2004; Choi, 2010, 2011) and upper-point-bar deposits are commonly considered the most prone to preserve tidal rhythmicity (Lanier & Tessier, 1998; Choi, 2010, 2011; Sisulak & Dashtgard, 2012; La Croix & Dashtgard, 2015; Pelletier *et al.*, 2016). In the 2012 accretionary package, the occurrence of thickening – thinning NS sequences in cores 3 and 4 and their absence at the same elevation in cores 2, 5 and 6, points out that preservation of tidal signature is also influenced by position along the meander bend. Rhythmites are common in the bend-apex zone, where development of the low-energy area, caused accumulation of thicker and mud-rich point-bar deposits. In this shadow zone, currents were not able to remove slack-water mud drapes and allowed preservation of thickening – thinning NS sequences at different elevations within the point bar. At core sites 3 and 4, preservation of thickening – thinning NS sequences in the lower part of the point bar could also be ascribed to sedimentation within a local scour (Fig. 13), where protected conditions promoted preservation of muddy laminae. lidar data also show that in the bend-apex zone, ebb-oriented and flood-oriented current ripples can coexist on a limited area (Fig. 11); whereas in the landward and

seaward sides of the point bar only limited unidirectional seaward-migrating and landward-migrating current ripples occur, respectively. Although lidar data were only acquired at the end of the ebb-phase, coexistence of ebb and flood-oriented ripples in the bend apex zone seems to suggest that this area is the site where bidirectional bedforms tend to develop, in comparison with point-bar sides.

Underestimating the dominance of tidal currents in the rock record is a relevant problem, and the overall scarcity of NS sequences in the deposits of one of the most famous hypertidal environments, such as the Mont-Saint-Michel Bay, confirms that. Nevertheless, the results of the present study point out that location of the deposits along a tidal band can play a key role in controlling preservation of tidal signature. Point bar bodies formed in similar settings potentially show an extreme vertical and lateral variability in sedimentary facies, with depositional and erosional processes dominating the bend-apex zone and the point-bar sides, respectively. Tidal signature, mud abundance and thicker deposits should be found in the apex-zone; whereas erosional surfaces, coarser-grained sediments and thinner deposits should be more frequent elsewhere along the point bar (Fig. 14).

CONCLUSIONS

A hypertidal point bar belonging to the upper-intertidal domain of the Mont-Saint-Michel Bay (France) was analysed by means of an integrated approach, which included time-series lidar topographic data, used to create a synthetic stratigraphy of the point bar, geomorphological field surveys and sedimentological core data. Studied point-bar deposits were accreted along the inner bank between 28 March 2012 and 29 November 2012, and were analysed in terms of their spatial distribution, grain size, thickness and preservation of tidal signature. Furthermore, this short-term analysis was contextualized within the decennial timescale evolution of the related tidal channel, which in the last two decades mainly followed an expansional and seaward planform transformation.

The reconstructed synthetic stratigraphy allowed the authors to detect that, in the considered time interval, the study bend expanded increasing channel sinuosity. However, bend expansion was not achieved by a progressive increase in sinuosity due to a uniform sediment distribution along the associated point bar, but occurred through alternating stages of sediment storage along the seaward and landward sides of the point bar. These processes were probably triggered by short-term complex morphodynamic processes, causing a local dominance of flood and ebb currents in different portions of the point bar.

Deposits accumulated between 28 March 2012 and 29 November 2012 formed an accretionary package of *ca* 3300 m^3 and were mainly deposited in the point-bar-slope zone forming an arcuate sedimentary body, covering the pre-existing point-bar morphology. The maximum sediment accumulation occurred in the point-bar-apex zone, where the maximum mud deposition also occurred. This study suggests that the development of a low-energy zone at the point-bar apex due to flow configuration, tidal asymmetry, and the mutually evasive nature of flood and ebb flows in meandering channels, is responsible for the enhanced sediment accumulation and mud deposition in this area. In the bend apex, tidal currents were not able to remove slack-water mud and also allowed preservation of tidal rhythmites at different elevations within the point bar. Accumulation within localized scours enhanced preservation of rhythmites also in the lower part of the point bar, where, commonly, mud drapes are removed by currents. This study shows that location of the deposits along the point bar plays a crucial role in preservation of tidal signature, and highlights the importance of depicting along-bar facies trends to develop predictive facies models and detect ancient tidal point bars in the stratigraphic record.

ACKNOWLEDGEMENTS

This study was supported by: University of Padova (SID2016 project, "From channels to rock record: morphodynamic evolution of tidal meanders and related sedimentary products" (P.I. M. Ghinassi); CARIPARO Fundation (HYDROSEM project; Progetto di Eccellenza CARIPARO 2017, "Fluvial and tidal meanders of the Venetian-Po Plain: from hydrodynamics to stratigraphy" – P.I. M. Ghinassi). The Titan airborne lidar sensor, operated by the Nantes-Rennes lidar Platform has been funded by the Region Pays de la Loire with funding of the RS2E-OSUNA programs and the Region Bretagne with support from the European Regional Development Fund. MC acknowledges the support by the 'Bourses de recherche du gouvernement

français (2017/2018) – Bourses de mobilité pour doctorants' which funded a three-month stay at the Université de Rennes. DL and JL acknowledge project funding from CNRS/EC2CO/PNEC for terrestrial lidar acquisition. Alain Crave is greatly acknowledged for helping in setting up flow velocity measurements in the study site. The authors thank Chief Editor Ian Kane, Associate Editor Piret Plink-Björklund, and reviewers Valentina Marzia Rossi, Janrik van den Berg and Bernadette Tessier for their thoughtful reviews, which have improved the article. Open Access Funding provided by Universita degli Studi di Padova within the CRUI-CARE Agreement.

CONFLICT OF INTEREST

The authors declare that they have no known competing financial interests or personal relationships that could have appeared to influence the work reported in this paper.

DATA AVAILABILITY STATEMENT

The data that support the findings of this study are available from the corresponding author upon reasonable request.

REFERENCES

Ahnert, F. (1960) Estuarine Meanders in the Chesapeake Bay Area. *Geogr. Rev*, **50**, 390–401.

Allen, J.R.L. (1982) *Sedimentary Structures. Their Character and Physical Basis*, Volume **I** (pp. 1–593). Elsevier, Amsterdam.

Archer, A.W. (1998) Hierarchy of Controls on Cyclic Rhythmite Deposition: Carboniferous Basins of Eastern and Mid-Continental U.S.A. *Tidalites Process. Prod. SEPM SP*, **61**, 59–68.

Archer, A.W. (2013) World's highest tides: Hypertidal coastal systems in North America, South America and Europe. *Sediment. Geol.*, **284–285**, 1–25.

Barwis, J.H. (1978) Sedimentology of some South Carolina tidal-creek point bars, and a comparison with their fluvial counterparts. In: *Fluvial Sedimentology, Canadian S* (Ed. Miall, A.D.), *Dallas Geological Society, Calgary, Alberta, Canada*, **5**, 487–510.

Billeaud, I., **Tessier, B.**, **Lesueur, P.** and **Caline, B.** (2007) Preservation potential of highstand coastal sedimentary bodies in a macrotidal basin: Example from the Bay of Mont-Saint-Michel, NW France. *Sediment. Geol*, **202**, 754–775.

Billeaud, I., **Tessier, B.** and **Lesueur, P.** (2009) Impacts of late Holocene rapid climate changes as recorded in a macrotidal coastal setting (Mont-Saint-Michel Bay, France). *Geology*, **37**, 1031–1034.

Boersma, J.R. and **Terwindt, J.H.J.** (1981) Neap–spring tide sequences of intertidal shoal deposits in a mesotidal estuary. *Sedimentology*, **28**, 151–170.

Bonnot-Courtois, C. (2012) Dynamique sédimentaire intertidale en baie du Mont-Saint- Michel entre évolution naturelle et aménagements. In: *XIIèmes Journées*, pp. 187–222. Paralia, Cherbourg.

Bonnot-Courtois, C. (2020) Intertidal sedimentary dynamics in Mont-Saint-Michel bay, a study of its natural evolution and man-made modifications. *Rev. Paralia*, **13**, n02.1–n02.34.

Bonnot-Courtois, C., **Caline, B.**, **L'Homer, A.** and **LeVot, M.** (2002) *Bay of Mont-Saint-Michel and the Rance Estuary: Recent Development and Evolution of the Depositional Environments*. Bulletin du Centre de recherche Elf Exploration et Production, Pau, 256 pp.

Bonnot-courtois, C. and **Levasseur, J.E.** (2012) Organisation générale de la végétation littorale des estrans vaseux. In: *Manuel D'étude et de Gestion Des Oiseaux et de Leurs Habitats En Zone Côtière*, 23–60.

Bourcart, J. and **Charlier, R.** (1959) The tangue: A "nonconforming" sediment. *Geol. Soc. Am. Bull*, **70**, 565–568.

Braat, L., **van Dijk, W.M.**, **Pierik, H.J.**, **van de Lageweg, W.**, **Bruckner, M.**, **Wagner-Cremer, F.** and **Kleinhans, M.G.** (2019) Tidal bar accretion by mudflat sedimentation. *EarthArXiv Prepr.*, August 29, 1–47.

Bridges, P.H. and **Leeder, M.R.** (1976) Sedimentary model for intertidal mudflat channels, with examples from the Solway Firth, Scotland. *Sedimentology*, **23**, 533–552.

Brivio, L., **Ghinassi, M.**, **D'Alpaos, A.**, **Finotello, A.**, **Fontana, A.**, **Roner, M.** and **Howes, N.** (2016) Aggradation and lateral migration shaping geometry of a tidal point bar: An example from salt marshes of the Northern Venice Lagoon (Italy). *Sediment. Geol.*, **343**, 141–155.

Broughton, P.L. (2018) Mudstone Clast Breccia in the Cretaceous Athabasca Oil Sands, Western Canada: Fluvial Debris-Flow Transitions into Traction Carpets. *J. Geol.*, **126**, 63–97.

Caline, B., **Larsonneur, C.** and **L'Homer, A.** (1982) La baie du Mont- Saint-Michel: principaux environnements sédimentaires. *Mém. Géol. Univ. Dijon. Livre Jubil. Gabriel Lucas*, **7**, 37–52.

Carling, P.A., **Chateau, C.C.**, **Leckie, D.A.**, **Langdon, C.T.**, **Scaife, R.G.** and **Parsons, D.R.** (2015) Sedimentology of a tidal point-bar within the fluvial-tidal transition: River Severn Estuary, UK. In: *Developments in Sedimentology*, 1st edn (Eds Ashworth, P.J., Best, J.L. and Parsons, D.R.), *Elsevier B.V.*, **68**, 149–189.

Changxing, S., **Petts, G.** and **Gurnell, A.** (1999) Bench development along the regulated, lower river Dee, UK. *Earth Surf. Process. Landforms*, **24**, 135–149.

Chen, S., **Steel, R.J.** and **Olariu, C.** (2015) Palaeo-Orinoco (Pliocene) channels on the tide-dominated Morne L'Enfer delta lobes and estuaries, SW Trinidad. In: *Developments in Sedimentology*, 1st edn (Eds Ashworth, P.J., Best, J.L. and Parsons, D.R.), *Elsevier B.V.*, **68**, 227–281.

Choi, K. (2010) Rhythmic Climbing-Ripple Cross-Lamination in Inclined Heterolithic Stratification (IHS) of a Macrotidal Estuarine Channel, Gomso Bay, West Coast of Korea. *J. Sediment. Res.*, **80**, 550–561.

Choi, K. (2011) Tidal rhythmites in a mixed-energy, macrotidal estuarine channel, Gomso Bay, west coast of Korea. *Mar. Geol.*, **280**, 105–115.

Choi, K.S. and **Dalrymple, R.W.** (2004) Recurring tide-dominated sedimentation in Kyonggi Bay (west coast of Korea): similarity of tidal deposits in late Pleistocene and Holocene sequences. *Mar. Geol.*, **212**, 81–96.

Choi, K.S., **Dalrymple, R.W.**, **Chun, S.S.** and **Kim, S.-P.-S.-P.-S.** (2004) Sedimentology of modern, Inclined Heterolithic Stratification (IHS) in the macrotidal Han River Delta, Korea. *J. Sediment. Res*, **74**, 677–689.

Choi, K.S., **Hong, C.M.**, **Kim, M.H.**, **Oh, C.R.** and **Jung, J.H.** (2013) Morphologic evolution of macrotidal estuarine channels in Gomso Bay, west coast of Korea: Implications for the architectural development of inclined heterolithic stratification. *Mar. Geol.*, **346**, 343–354.

Choi, K.S. and **Jo, J.H.** (2015) Morphodynamics of Tidal Channels in the Open Coast Macrotidal Flat, Southern Ganghwa Island in Gyeonggi Bay, West Coast of Korea. *J. Sediment. Res*, **85**, 582–595.

Choi, K.S. and **Park, Y.A.** (2000) Late Pleistocene silty tidal rhythmites in the macrotidal flat between Youngjong and Yongyou Islands, west coast of Korea. *Mar. Geol.*, **167**, 231–241.

Cleveringa, J. and **Oost, A.P.** (1999) The fractal geometry of tidal-channel systems in the Dutch Wadden Sea. *J. Geosci.*, **78**, 21–30.

Cosma, M., **Finotello, A.**, **Ielpi, A.**, **Ventra, D.**, **Oms, O.**, **D'Alpaos, A.** and **Ghinassi, M.** (2020) Piracy-controlled geometry of tide-dominated point bars: Combined evidence from ancient sedimentary successions and modern channel networks. *Geomorphology*, **370**, 107402.

Cosma, M., **Ghinassi, M.**, **D'Alpaos, A.**, **Roner, M.**, **Finotello, A.**, **Tommasini, L.** and **Gatto, R.** (2019) Point-bar brink and channel thalweg trajectories depicting interaction between vertical and lateral shifts of microtidal channels in the Venice Lagoon (Italy). *Geomorphology*, **342**, 37–50.

Cosma, M., **Yan, N.**, **Colombera, L.**, **Mountney, N.P.**, **D'Alpaos, A.** and **Ghinassi, M.** (2021) An integrated approach to determine three-dimensional accretion geometries of tidal point bars: Examples from the Venice Lagoon (Italy). *Sedimentology*, **68**, 449–476.

Couëffé, R., **Tessier, B.**, **Gigot, P.** and **Beaudoin, B.** (2004) Tidal rhythmites as possible indicators of very rapid subsidence in a foreland basin: An example from the Miocene Marine Molasse Formation of the Digne foreland basin, SE France. *J. Sediment. Res*, **74**, 2–15.

Cuevas Gonzalo, M. (1991) Tide-influenced fluvial deposits; Examples from the Eocene of the Southern Pyrenees, Spain. In: *4th International Conference on Fluvial Sedimantology* (Eds Marzo, M. and Puigdefabregas, C.), pp. 1–93. Servei Geologic de Catalunya, Barcelona

D'Alpaos, A., **Ghinassi, M.**, **Finotello, A.**, **Brivio, L.**, **Bellucci, L.G.** and **Marani, M.** (2017) Tidal meander migration and dynamics: A case study from the Venice Lagoon. *Mar. Pet. Geol*, **87**, 80–90.

Dalrymple, R.W. and **Choi, K.S.** (2007) Morphologic and facies trends through the fluvial-marine transition in tide-dominated depositional systems: A schematic framework for environmental and sequence-stratigraphic interpretation. *Earth-Science Rev*, **81**, 135–174.

Dalrymple, R.W., **Makino, Y.** and **Zaitlin, B.A.** (1991) Temporal and spatial patterns of rhythmite deposition on mud flats in the macrotidal Cobequid Bay-Salmon River estuary. Bay of Fundy, Canada. In: *Clastic Tidal Sedimentology* (Eds Smith, D.G., Reinson, G.E., Zaitlin, B.A. and Rahmani, R.A.), *Canadian Society of Petroleum Geologists, Calgary, Memoir*, **16**, 137–160.

Davis, R.A. (2012) Tidal Signatures and Their Preservation Potential in Stratigraphic Sequences. In: *Principles of Tidal Sedimentology* (Eds Davis, R.A. and Dalrymple, R.W.), pp. 1–621. Springer, Dordrecht.

De Mowbray, T. (1983) The genesis of lateral accretion deposits in recent intertidal mudflat channels, Solway Firth, Scotland. *Sedimentology*, **30**, 425–435.

Desguée, R. (2008) *Etude des processus hydro-sédimentaires et évolutions morphodynamiques autour du Mont-Saint-Michel*. Université de Caen, Caen.

Desguée, R., **Robin, N.**, **Gluard, L.**, **Monfort, O.**, **Anthony, E.J.** and **Levoy, F.** (2011) Contribution of hydrodynamic conditions during shallow water stages to the sediment balance on a tidal flat: Mont-Saint-Michel Bay, Normandy, France. *Estuar. Coast. Shelf Sci*, **94**, 343–354.

Détriché, S., **Susperregui, A.-S.**, **Feunteun, E.**, **Lefeuvre, J.-C.** and **Jigorel, A.** (2011) Interannual (1999–2005) morphodynamic evolution of macro-tidal salt marshes in Mont-Saint-Michel Bay (France). *Cont. Shelf Res.*, **31**, 611–630.

Díez-Canseco, D., **Arz, J.A.**, **Benito, M.I.**, **Díaz-Molina, M.**, **Arenillas, I.**, **Benito, J.I.**, **Díaz-Molina, M.** and **Arenillas, I.** (2014) Tidal influence in redbeds: A palaeoenvironmental and biochronostratigraphic reconstruction of the Lower Tremp Formation (South-Central Pyrenees, Spain) around the Cretaceous/Paleogene boundary. *Sediment. Geol.*, **312**, 31–49.

EDF R&D, T.P. (2011) Cloud Compare (version 2.4) [GPL software] http://www.danielgm.net/cc/.

Fagherazzi, S., **Gabet, E.J.** and **Furbish, D.J.** (2004) The effect of bidirectional flow on tidal channel planforms. *Earth Surf. Process. Landforms*, **29**, 295–309.

Fenies, H. and **Faugères, J.C.** (1998) Facies and geometry of tidal channel-fill deposits (Arcachon Lagoon, SW France). *Mar. Geol.*, **150**, 131–148.

Ferguson, R.I., **Parsons, D.R.**, **Lane, S.N.** and **Hardy, R.J.** (2003) Flow in meander bends with recirculation at the inner bank. *Water Resour. Res.*, **39**, 1322.

Finotello, A., **Lanzoni, S.**, **Ghinassi, M.**, **Marani, M.**, **Rinaldo, A.**, **D'Alpaos, A.** and **D'Alpaos, A.** (2018) Field migration rates of tidal meanders recapitulate fluvial morphodynamics. *Proc. Natl. Acad. Sci*, **115**, 201711330.

Fruergaard, M., **Andersen, T.J.**, **Nielsen, L.H.**, **Madsen, A.T.**, **Johannessen, P.N.**, **Murray, A.S.**, **Kirkegaard, L.** and **Pejrup, M.** (2011) Punctuated sediment record resulting from channel migration in a shallow sand-dominated micro-tidal lagoon, Northern Wadden Sea, Denmark. *Mar. Geol*, **280**, 91–104.

Furgerot, L., **Mouazé, D.**, **Tessier, B.**, **Perez, L.** and **Haquin, S.** (2013) Suspended sediment concentration in relation to the passage of a tidal bore (See River). *Coast. Dyn.*, 671–682.

Fustic, M., **Hubbard, S.M.**, **Spencer, R.**, **Smith, D.G.**, **Leckie, D.A.**, **Bennett, B.** and **Larter, S.** (2012) Recognition of down-valley translation in tidally influenced meandering fluvial deposits, Athabasca Oil Sands (Cretaceous), Alberta, Canada. *Mar. Pet. Geol.*, **29**, 219–232.

Gabet, E.J. (1998) Lateral Migration and Bank Erosion in a Saltmarsh. *Estuaries*, **21**, 745–753.

Garofalo, D. (1980) The Influence of Wetland Vegetation on Tidal Stream Channel Migration and Morphology. *Estuaries*, **3**, 258–270.

Garotta, V., **Rummel, A.C.** and **Seminara, G.** (2007) Long-term morphodynamics and hydrodynamics of tidal meandering channels. In: *5th IAHR Symposium on River, Coastal and Estuarine Morphodynamics*, **1**, 163–168.

Ghinassi, M., **Brivio, L.**, **D'Alpaos, A.**, **Finotello, A.**, **Carniello, L.**, **Marani, M.** and **Cantelli, A.** (2018a) Morphodynamic evolution and sedimentology of a microtidal meander bend of the Venice Lagoon (Italy). *Mar. Pet. Geol.*, **96**, 391–404.

Ghinassi, M., **D'Alpaos, A.**, **Gasparotto, A.**, **Carniello, L.**, **Brivio, L.**, **Finotello, A.**, **Roner, M.**, **Franceschinis, E.**, **Realdon, N.**, **Howes, N.** and **Cantelli, A.** (2018b) Morphodynamic evolution and stratal architecture of translating tidal point bars: Inferences from the northern Venice Lagoon (Italy). *Sedimentology*, **65**, 1354–1377.

Gingras, M.K., **Maceachern, J.A.**, **Dashtgard, S.E.**, **Ranger, M.J.** and **Pemberton, G.S.** (2016) The significance of trace fossils in the McMurray Formation, Résumé. *Bull. Cana.*, **64**, 233–250.

Gugliotta, M., **Saito, Y.**, **Nguyen, V.L.**, **Ta, T.K.O.**, **Tamura, T.** and **Fukuda, S.** (2018) Tide- and River-Generated Mud Pebbles from the Fluvial To Marine Transition Zone of the Mekong River Delta, Vietnam. *J. Sediment. Res.*, **88**, 981–990.

Harris, P.T., **Hughes, M.G.**, **Baker, E.K.**, **Dalrymple, R.W.** and **Keene, J.B.** (2004) Sediment transport in distributary channels and its export to the pro-deltaic environment in a tidally dominated delta: Fly River, Papua New Guinea. *Cont. Shelf Res.*, **24**, 2431–2454.

Hovikoski, J., **Räsänen, M.**, **Gingras, M.**, **Ranzi, A.** and **Melo, J.** (2008) Tidal and seasonal controls in the formation of Late Miocene inclined heterolithic stratification deposits, western Amazonian foreland basin. *Sedimentology*, **55**, 499–530.

Hubbard, S.M., **Smith, D.G.**, **Nielsen, H.**, **Leckie, D.A.**, **Fustic, M.**, **Spencer, R.J.** and **Bloom, L.** (2011) Seismic geomorphology and sedimentology of a tidally influenced river deposit, Lower Cretaceous Athabasca oil sands, Alberta, Canada. *Am. Assoc. Pet. Geol. Bull*, **95**, 1123–1145.

Ichaso, A.A. and **Dalrymple, R.W.** (2009) Tide- and wave-generated fluid mud deposits in the Tilje Formation (Jurassic), offshore Norway. *Geology*, **37**, 539–542.

Jablonski, B.V.J.J.J. and **Dalrymple, R.W.** (2016) Recognition of strong seasonality and climatic cyclicity in an ancient, fluvially dominated, tidally influenced point bar: Middle McMurray Formation, Lower Steepbank River, north-eastern Alberta, Canada. *Sedimentology*, **63**, 552–585.

Johnson, S.M. and **Dashtgard, S.E.** (2014) Inclined heterolithic stratification in a mixed tidal-fluvial channel: Differentiating tidal versus fluvial controls on sedimentation. *Sediment. Geol*, **301**, 41–53.

Johnston, S. and **Holbrook, J.** (2019) Toggling between expansion and translation. In: *Fluvial Meanders and Their Sedimentary Products in the Rock Record* (Eds Ghinassi, M., Colombera, L., Mountney, N.P., Reesink, A.J. and Bateman, M.), pp. 47–80. John Wiley & Sons, Ltd, Hoboken.

Kazhdan, M., **Bolitho, M.** and **Hoppe, H.** (2006) Poisson surface reconstruction. In: *Eurographics Symposium on Geometry Processing* (Eds Polthier, K. and Sheffer, A.), pp. 1–10. The Eurographics Association, Geneve.

Kazhdan, M. and **Hoppe, H.** (2013) Screened Poisson Surface Reconstruction. *ACM Trans. Graph*, **32**, 1–13.

Kleinhans, M.G., **Schuurman, F.**, **Bakx, W.** and **Markies, H.** (2009) Meandering channel dynamics in highly cohesive sediment on an intertidal mud flat in the Westerschelde estuary, the Netherlands. *Geomorphology*, **105**, 261–276.

Knighton, A.D., **Mills, K.** and **Woodroffe, C.D.** (1991) Tidal-creek extension and saltwater intrusion in northern Australia. *Geology*, **19**, 831–834.

Kvale, E.P. (2012) Tidal Constituents of Modern and Ancient Tidal Rhythmites: Criteria for Recognition and Analyses. In: *Principles of Tidal Sedimentology* (Eds Davis, R.A. and Dalrymple, R.W.), pp. 1–17. Springer, Dordrecht.

Kvale, E.P., **Archer, A.W.** and **Johnson, H.R.** (1989) Daily, monthly, and yearly tidal cycles within laminated siltstones of the Mansfield Formation (Pennsylvanian) of Indiana. *Geology*, **17**, 365–368.

L'Homer, A., **Courbouleix, S.**, **Chantraine, J.**, **Deroin, J.P.**, **Bonnot-Courtois, C.**, **Caline, B.**, **Ehrhold, A.**, **Lautridou, J.P.** and **Morzadec-Kerfourn, M.T.** (1999) *Notice Explicative, Carte Géol. France (1/50 000), Feuille Baie Du Mont-Saint-Michel (208)*. BRGM, Orléans, 184 pp.

La Croix, A.D. and **Dashtgard, S.E.** (2014) Of sand and mud: Sedimentological criteria for identifying the turbidity maximum zone in a tidally influenced river. *Sedimentology*, **61**, 1961–1981.

La Croix, A.D. and **Dashtgard, S.E.** (2015) A Synthesis of Depositional Trends In Intertidal and Upper Subtidal Sediments Across the Tidal-Fluvial Transition In the Fraser River, Canada. *J. Sediment. Res.*, **85**, 683–698.

Lague, D., **Brodu, N.** and **Leroux, J.** (2013) Accurate 3D comparison of complex topography with terrestrial laser scanner: Application to the Rangitikei canyon (N-Z). *ISPRS J. Photogramm. Remote Sens.*, **82**, 10–26.

Langlois, E., **Bonis, A.** and **Bouzillé, J.B.** (2003) Sediment and plant dynamics in saltmarshes pioneer zone: Puccinellia maritima as a key species? *Estuar. Coast. Shelf Sci*, **56**, 239–249.

Lanier, W.P. and **Tessier, B.** (1998) Climbing-ripple bedding in the fluvio-estuarine transition: a common feature associated with tidal dynamics (modern and ancient analouges). In: *Tidalites: Processes and Products* (Eds Alexander, C., Davis, R.A. and Henry, V.J.), *SEPM Speci*, **61**, 109–117.

Larsonneur, C. (1975) Tidal Deposits, Mont Saint-Michel Bay, France. In: *Tidal Deposits* (Ed. Ginsburg, R.N.), pp. 21–30. Springer, Berlin, Heidelberg.

Larsonneur, C. (1989) La Baie du Mont-Saint-Michel. *Bull. lnst. Géol. Bassin Aquit*, **46**, 5–74.

Larsonneur, C., **Auffret, J.-P.**, **Caline, B.**, **Gruet, Y.** and **Lautridou, J.-P.** (1994) The Bay of Mont-Saint-Michel: A sedimentation model in a temperate macrotidal environment. *Senckenbergiana Maritima*, **24**, 3–63.

Leeder, M.R.R. and **Bridges, P.H.H.** (1975) Flow separation in meander bends. *Nature*, **253**, 338–339.

Legler, B., **Johnson, H.D.**, **Hampson, G.J.**, **Massart, B.Y.G.G.**, **Jackson, C.A.L.L.**, **Jackson, M.D.**, **El-Barkooky, A.** and **Ravnas, R.** (2013) Facies model of a fine-grained, tide-dominated delta: Lower Dir Abu Lifa Member (Eocene), Western Desert, Egypt. *Sedimentology*, **60**, 1313–1356.

Lentsch, N., **Finotello, A.** and **Paola, C.** (2018) Reduction of deltaic channel mobility by tidal action under rising relative sea level. *Geology*, **46**, 599–602.

Leopold, L.B., **Collins, J.N.** and **Collins, L.M.** (1993) Hydrology of some tidal channels in estuarine marshland near San Francisco. *Catena*, **20**, 469–493.

Leroux, J. (2013) *Chenaux tidaux et dynamique des prés-salés en régime méga-tidal: approche multi-temporelle du*

siècle à l'évènement de marée. Université de Rennes 1, Rennes.

Levoy, F., **Anthony, E.J.**, **Monfort, O.** and **Larsonneur, C.** (2000) The morphodynamics of megatidal beaches in Normandy, France. *Mar. Geol*, **171**, 39–59.

Levoy, F., **Anthony, E.J.**, **Dronkers, J.**, **Monfort, O.** and **Montreuil, A.-L.** (2019) Short-term to Decadal-scale Sand Flat Morphodynamics and Sediment Balance of a Megatidal Bay: Insight from Multiple LiDAR Datasets. *J. Coast. Res.*, **88**, 61–76.

Li, C., **Chen, C.**, **Guadagnoli, D.** and **Georgiou, I.Y.** (2008) Geometry-induced residual eddies in estuaries with curved channels: Observations and modeling studies. *J. Geophys. Res. Ocean*, **113**, 1–14.

Longhitano, S.G., **Mellere, D.**, **Steel, R.J.** and **Ainsworth, R.B.** (2012) Tidal depositional systems in the rock record: A review and new insights. *Sediment. Geol.*, **279**, 2–22.

Marani, M., **Lanzoni, S.**, **Zandolin, D.**, **Seminara, G.**, **Rinaldo, A.**, **Zandolin, D.**, **Lanzoni, S.**, **Marani, M.** and **Rinaldo, A.** (2002) Tidal meanders. *Water Resour. Res.*, **38**, 7–14.

Martinius, A.W. and **Van den Berg, J.H.** (2011) *Atlas of Sedimentary Structures in Estuarine and Tidally-Influenced River Deposits of the Holocene Rhine-Meuse-Scheldt System: Their Application to the Interpretation of Analogous Outcrop and Subsurface Depositional Systems*. EAGE publications, Houten, 298 pp.

Migniot (1997) *Rétablissement du caractère maritime du Mont-Saint-Michel. Synthèse des connaissances hydro-sédimentaires de la baie*. Technical Report unpublished, DDE Manche.

Musial, G., **Reynaud, J.Y.**, **Gingras, M.K.**, **Féniès, H.**, **Labourdette, R.** and **Parize, O.** (2012) Subsurface and outcrop characterization of large tidally influenced point bars of the Cretaceous McMurray Formation (Alberta, Canada). *Sediment. Geol.*, **279**, 156–172.

Nio, S.D. and **Yang, C.S.** (1991) Sea-level fluctuations and the geometric variability of tide-dominated sandbodies. *Sediment. Geol.*, **70**(2–4), 161–193.

Olariu, C., **Steel, R.J.**, **Olariu, M.I.** and **Choi, K.** (2015) Facies and architecture of unusual fluvial–tidal channels with inclined heterolithic strata: Campanian Neslen Formation, Utah, USA. In: *Developments in Sedimentology*, Volume **68**, 1st edn (Eds Ashworth, P.J., Best, J.L. and Parsons, D.R.), pp. 353–394. Elsevier, Amsterdam.

Pearson, N.J. and **Gingras, M.K.** (2006) An Ichnological and Sedimentological Facies Model for Muddy Point-Bar Deposits. *J. Sediment. Res*, **76**, 771–782.

Pelletier, J., **Abouessa, A.**, **Schuster, M.**, **Duringer, P.** and **Rubino, J.-L.** (2016) Hierarchy of tidal rhythmites from semidiurnal to solstitial cycles: Origin of inclined heterolithic stratifications (IHS) in tidal channels from the Dur At Talah Formation (upper Eocene, Sirte Basin, Libya) and a facies comparison with modern Mont-Saint-Michel Bay deposits (France). In: *Contributions to Modern and Ancient Tidal Sedimentology: Proceedings of the Tidalites 2012 Conference* (Eds Tessier, B. and Reynaud, J.-Y.), *IAS SP*, **47**, 203–216.

Rebata, L.A., **Gingras, M.K.**, **Räsänen, M.E.** and **Barberi, M.** (2006) Tidal-channel deposits on a delta plain from the upper miocene nauta formation, Marañón Foreland Sub-basin, Peru. *Sedimentology*, **53**, 971–1018.

Reineck, H.-E. (1970) *Das Watt: Ablagerungs- und Lebensraum*. Kramer, Senckenberg Institute, Frankfurt am Main.

Riley, S.J. and **Taylor, G.** (1978) The geomorphology of the upper Darling River system with special reference to the present fluvial system. *Proc. R. Soc. Victoria*, **90**, 89–102.

Robinson, A.H.W. (1960) Ebb-flood Channel Systems in Sandy Bays and Estuaries. *Geography*, **45**, 183–199.

Rossi, V.M., **Perillo, M.M.**, **Steel, R.J.** and **Olariu, C.** (2017) Quantifying Mixed-Process Variability In Shallow-Marine Depositional Systems: What Are Sedimentary Structures Really Telling Us? *J. Sediment. Res*, **87**, 1060–1074.

Roux, P. (1998) Rapport sur les niveaux de la mer aux abords du Mont-Saint-Michel. Données de 1884 à 1998.

Santos, A.E.D.A. and **Rossetti, D.D.F.** (2006) Depositional model of the Ipixuna Formation (Late Cretaceous-?Early Tertiary), Rio Capim Area, northern Brazil. *Lat. Am. J. Sedimentol. Basin Anal*, **13**, 101–117.

Simon, S.S.T., **Gibling, M.R.**, **Dimichele, W.A.**, **Chaney, D.S.** and **Koll, R.** (2019) An exhumed fine-grained meandering channel in the lower Permian Clear Fork Formation , north-central Texas: Processes of mud accumulation and the role of vegetation in channel dynamics. In: *Fluvial Meanders and Their Sedimentary Products in the Rock Record* (Eds Ghinassi, M., Colombera, L., Mountney, N.P., Reesink, A.J. and Bateman, M.), pp. 149–172. John Wiley & Sons, Ltd, Hoboken.

Sisulak, C.F. and **Dashtgard, S.E.** (2012) Seasonal Controls On the Development And Character of Inclined Heterolithic Stratification In A Tide-Influenced, Fluvially Dominated Channel: Fraser River, Canada. *J. Sediment. Res*, **82**, 129.

Smith, D.G. (1987) Meandering river point bar lithofacies models: modern and ancient examples compared. In: *Recent Developments in Fluvial Sedimentology: Contributions from the Third International Fluvial Sedimentology Conference* (Eds Ethridge, F.G., Flores, R.M. and Harvey, M.D.), *SEPM Society for Sedimentary Geology*, **39**, 83–91.

Solari, L., **Seminara, G.**, **Lanzoni, S.**, **Marani, M.** and **Rinaldo, A.** (2002) Sand bars in tidal channels Part 2. Tidal meanders. *J. Fluid Mech.*, **451**, 203–238.

Terwindt, J.H.J. (1988) Palaeotidal reconstructions of inshore tidal depositional environments. In: *Tide-Influenced Sedimentary Environments and Facies* (Eds De Boer, P.L., van Gelder, A. and Nio, S.-D.), pp. 233–263. D. Reidel Publishing Company, Dordrecht.

Tessier, B. (1993) Upper intertidal rhythmites in the Mont-Saint-Michel Bay (NW France): Perspectives for paleoreconstruction. *Mar. Geol.*, **110**, 355–367.

Tessier, B. (1998) Tidal cycles: Annual versus semi-lunar records. In: *Tidalites: Processes and Products* (Eds Alexander, C. and Henry, V.J.), *SEPM Society for Sedimentary Geology*, **61**, 69–74.

Tessier, B., **Billeaud, I.** and **Lesueur, P.** (2010) Stratigraphic organisation of a composite macrotidal wedge: The Holocene sedimentary infilling of the Mont-Saint-Michel Bay (NW France). *Bull. la Soc. Geol. Fr*, **181**, 99–113.

Tessier, B., **Furgerot, L.** and **Mouazé, D.** (2017) Sedimentary signatures of tidal bores: a brief synthesis. *Geo-Marine Lett*, **37**, 325–331.

Tessier, B. and **Gigot, P.** (1989) A vertical record of different tidal cyclicities: an example from the Miocene Marine Molasse of Digne (Haute Provence, France). *Sedimentology*, **36**, 767–776.

Tessier, M., **Gloaguen, J.C.** and **Lefeuvre, J.C.** (2000) Factors affecting the population dynamics of Suaeda maritima at initial stages of development. *Plant Ecol.*, **147**, 193–203.

Thomas, R.G., **Smith, D.G.**, **Wood, J.M.**, **Visser, M.J.**, **Calverley-Range, E.A.**, **Koster, E.H.**, **Visser, J.**, **Calverley-Range, E.A.** and **Koster, E.H.** (1987) Inclined heterolithic stratification - terminology, description, interpretation and significance. *Sediment. Geol.*, **53**, 123–179.

Thoms, M.C. and **Sheldon, F.** (1996) The importance of channel complexity for ecosystem processing: An example of the Barwon-Darling River. *Stream Manag. Aust.*, 111–118.

Van de Lageweg, W.I., **van Dijk, W.M.**, **Kleinhans, M.G.** and **Utrecht, U.** (2013) Channel belt architecture formed by a meandering river. *Sedimentology*, **60**, 840–859.

Van den Berg, J.H. (1981) Rhythmic Seasonal Layering in a Mesotidal Channel Fill Sequence, Oosterschelde Mouth, the Netherlands. *Spec. Publ. int. Ass. Sediment*, **5**, 147–159.

Van den Berg, J.H., **Jeuken, M.C.J.L.** and **Van der Spek, A.J.F.** (1996) Hydraulic processes affecting the morphology and evelotion of the Westerschelde estuary. In: *Estuarine Shores: Evolution, Environments and Human Alterations* (Eds Nordstrom, K.F. and Roman, C.T.), pp. 157–183. John wiley & Sons Ltd, Hoboken.

Van Straaten, L.M.J.U. (1954) Composition and structure of recent marine sediments in the Netherlands. *Leidse Geol. Meded*, **19**, 1–108.

Van Straaten, L.M.J.U. (1964) De bodem der Waddenzee. In: *Het Waddenboek* (Eds Anderson, W.F., Abrahamse, J., Buwalda, J.D. and Van Straaten, L.M.J.U.), pp. 75–151. Thieme, Zutphen.

Van Veen, J. (1950) Eb- en vloedscharen in de Nederlandse getijwateren. *Tijdschrtft K. Ned. Aardrtjkskundig Genoot*, **67**, 303–335.

Woodroffe, C.D., **Chappell, J.M.A.**, **Thom, B.G.** and **Wallensky, E.** (1986) *Geomorphological Dynamics and Evolution of the South Alligator Tidal River and Plains, Northern Territory*. Australian National University, North Australia, 190 pp.

Woodyer, K.D., **Taylor, G.** and **Crook, K.A.W.** (1979) Depositional processes along a very low-gradient, suspended-load stream: the Barwon River, New South Wales. *Sediment. Geol.*, **22**, 97–120.

Zeff, M.L. (1999) Salt marsh tidal channel morphometry: Applications for wetland creation and restoration. *Restor. Ecol.*, **7**, 205–211.

Manuscript received 10 April 2020; revision 7 June 2021; revision accepted 25 August 2021